

# Open-source library for performance-portable neutrino reaction rates: Application to neutron star mergers

Leonardo Chiesa,<sup>1,2,\*</sup> Maitraya Bhattacharyya,<sup>3,4</sup> Filippo Mazzini,<sup>1,2</sup>  
Federico Maria Guercilena,<sup>1,2</sup> Albino Perego,<sup>1,2</sup> and David Radice<sup>3,5</sup>

<sup>1</sup>*Dipartimento di Fisica, Università di Trento, via Sommarive 14, 38123 Trento, Italy*

<sup>2</sup>*INFN-TIFPA, Trento Institute for Fundamental Physics and Applications, via Sommarive 14, 38123 Trento, Italy*

<sup>3</sup>*Institute for Gravitation & the Cosmos, The Pennsylvania State University, University Park, Pennsylvania 16802, USA*

<sup>4</sup>*Department of Physics, The Pennsylvania State University, University Park, Pennsylvania 16802, USA*

<sup>5</sup>*Department of Astronomy & Astrophysics, The Pennsylvania State University, University Park, Pennsylvania 16802, USA*

A realistic and detailed description of neutrinos in binary neutron star (BNS) mergers is essential to build reliable models of such systems. To this end, we present BNS\_NURATES, a novel open-source numerical library designed for the efficient on-the-fly computation of neutrino interactions, with particular focus on regimes relevant to BNS mergers. BNS\_NURATES targets a higher level of accuracy and realism in the implementation of commonly employed reactions by accounting for relevant microphysics effects on the interactions, such as weak magnetism and mean field effects. It also includes the contributions of inelastic neutrino scattering off electrons and positrons and (inverse) nucleon decays. Finally, it offers a way to reconstruct the neutrino distribution function in the framework of moment-based transport schemes. As a first application, we compute both energy-dependent and energy-integrated neutrino emissivities and opacities for conditions extracted from a BNS merger simulation with M1 transport scheme. We find some qualitative differences in the results when considering the impact of the additional relevant reactions and of microphysics effects. For example, neutrino-electron/positron scattering reactions are important for the energy exchange of heavy-type neutrinos as they do not undergo semileptonic charged-current processes, when  $\mu^\pm$  are not accounted for. Moreover, weak magnetism and mean field effects can significantly modify the contribution of  $\beta$  processes for electron-type (anti)neutrinos, increasing at the same time the importance of (inverse) neutron decays. The improved treatment for the reaction rates also modifies the conditions at which neutrinos decouple from matter in the system, potentially affecting their emission spectra.

## I. INTRODUCTION

The inclusion of detailed and realistic microphysics input in the description of binary neutron star (BNS) mergers is crucial to construct reliable models that can be compared with astrophysical observations. Among the different aspects to be considered, the interplay between neutrinos and nuclear matter must be modeled accurately as it may generate some distinct fingerprints on the dynamics of the coalescence (see, for example, [1] for a recent review). In particular, neutrinos transport and redistribute energy and momentum while diffusing across the system, see, e.g., [2–6]. As a consequence, they can affect the properties and the stability of the remnant, see, e.g., [7–9], possibly influencing the emission of gravitational waves in the merger aftermath [10–12]. In the high-density core of a noncollapsed remnant, they may also form a trapped and degenerate gas that contributes in a nontrivial way to the total pressure support of the system [9–11, 13, 14]. Neutrino interactions are also a critical input as they set the neutron-to-proton content of ejected matter, with direct consequences on the nucleosynthesis yields and on the associated kilonova signal [10, 15–24]. Recent studies have highlighted how the ejecta properties and in particular the degree of leptonization depend

on the neutrino transport and on the neutrino-matter interactions, see, e.g., [25–28]. This can, for example, affect the production of light elements by BNS coalescences, which may have been historically underestimated as a result of the approximated neutrino treatment, see, e.g., [29–31]. Other aspects concerning the role of neutrinos in the context of BNS mergers include the possible involvement in the formation of relativistic jets [2, 5, 32–35] and the occurrence of flavor-changing oscillations on time scales and length scales relevant for the dynamics and for the matter ejection, see, e.g., [36–42]. Finally, the characterization and possible detection of neutrino emission from BNS mergers is also an item of interest in its own right [43].

Neutrinos are numerically evolved in BNS merger simulations by approximately solving the Boltzmann transport equation. First attempts to include neutrino physics in BNS mergers relied on leakage schemes or on hybrid schemes that coupled leakage prescriptions for the optically thick regime and ray tracing or moment schemes for the optically thin regime, see, e.g., [3, 4, 6, 18, 20, 44, 45]. Recently, there have been some efforts aimed at improving the precision and reliability of employed transport schemes in BNS mergers by means of two-moment schemes [10, 46–51] or Monte Carlo based ones [52–56]. Along with a robust transport scheme, feeding accurate neutrino rates into the source term of the transport equation is of paramount importance for modeling the cor-

---

\* [leonardo.chiesa@unitn.it](mailto:leonardo.chiesa@unitn.it)

rect neutrino dynamics, particularly in the regions where neutrinos transition from equilibrium conditions to free-streaming propagation. Dedicated software libraries have been designed for such a purpose, e.g., [57, 58], often resting upon the expertise that has accumulated in the modeling of core-collapse supernovae (CCSNe). Recent studies have highlighted the importance of detailed microphysics to predict neutrino emissivities and absorptivities in hot and dense matter with high accuracy [59–66]. Possible relevant effects for the rate calculations of both neutral- and charged-current processes include full kinematics treatment, weak magnetism and pseudoscalar terms, energy-dependent nucleon form factors, and mean field energy shifts due to nuclear interactions. Another essential aspect is the inclusion of all of the relevant degrees of freedom, together with the most important associated reactions. In the context of BNS mergers, leptonic and semileptonic reactions involving muons should be also considered, see, e.g., [8, 9, 63, 64, 66, 67]. Despite these progresses, the characterization of neutrino interactions in neutron star mergers is still partial. Because of both an incomplete knowledge of the reaction rates and limitations in our computational capability, the description of the various reactions that are typically included in BNS merger modeling is often oversimplified, e.g., by adopting crude approximations on the matrix elements, by ignoring the impact of the surrounding nuclear medium, by assuming neutrinos in local thermodynamical equilibrium (LTE) conditions in any regime, or by relying on precomputed and tabulated rates, therefore introducing additional errors associated with interpolation procedures. Furthermore, the set of reactions that are considered is often not exhaustive, as there are processes whose impact in BNS merger conditions could be significant, but have not been explored yet in detail. As an example, the inelastic scattering of neutrinos off electrons and positrons (proven to be relevant for the dynamics of CCSNe and not usually included in BNS merger simulations), has been found by recent studies to be possibly impactful in the merger aftermath [68].

To tackle some of these issues, we have developed and present BNS\_NURATES, a novel open-source numerical library designed for the computation of neutrino-matter interaction rates in the regimes relevant for BNS mergers. This library provides an improved treatment of neutrino interactions, targeting a higher level of accuracy and realism compared to commonly employed neutrino rates prescriptions. BNS\_NURATES includes reactions that have not been extensively investigated in the context of BNS mergers, such as the inelastic neutrino-electron and neutrino-positron scattering and (inverse) nucleon decays. It also accounts for the impact of microphysics effects on some of the included interactions, such as recoil, phase-space and weak magnetism effects for scattering off nucleons, and  $\beta$  processes and in-medium effects for  $\beta$  processes. BNS\_NURATES is able to compute both spectral (energy-dependent) and gray (energy-integrated) neutrino emissivities and opacities for given

thermodynamic conditions, by prescribing a functional form for the distribution function of neutrinos. The library goes beyond the assumption of LTE conditions, as it reconstructs the neutrino distribution function starting from the information encoded in the first gray radiation moments, assuming a linear combination between the contribution of trapped and free-streaming neutrinos. Despite its focus on physical realism, the library has been designed to be computationally efficient in order to be coupled to transport schemes for the on-the-fly evaluation of neutrino opacities and emissivities, avoiding table interpolations. The computation is additionally accelerated thanks to the integration with the KOKKOS library, which allows to offload the evaluation at different grid points onto parallel graphical processing units (GPUs). BNS\_NURATES is publicly available [69] and will be actively maintained with the aim of further improving its accuracy, completeness and computational performance.

In this work we first discuss the physical content of BNS\_NURATES in terms of the neutrino-matter interactions and of the level of accuracy that it implements. We then apply BNS\_NURATES to the evaluation of both energy-dependent and energy-integrated neutrino emissivities and opacities for a set of thermodynamic conditions representative of the postmerger phase of a BNS system, extracted from a simulation employing a gray M1 neutrino transport scheme, in a postprocessing analysis. We discuss in detail what is the contribution of the different reactions and of microphysics effects in such conditions. Our goal is, on the one hand, to assess which processes are most relevant, and, on the other hand, to assess if the improved treatment could be impactful for the dynamics of neutrinos in the system.

We find that reactions and microphysics effects that are not always included in sophisticated simulations, but have been implemented into the library, have a significant impact on the total neutrino rates. In particular, we show that the inclusion of neutrino scattering off electrons and positrons provides an additional contribution to the opacity that is sizable wherever charged-current processes are not relevant, i.e., deep inside the remnant in the case of electron (anti)neutrinos and in general for heavy-type (anti)neutrinos. For the latter, we find that the emission spectrum is modified as their neutrino surfaces are pushed out to larger radii. Also mean field and weak magnetism effects prove to be influential, depending on the conditions. Mean field effects enhance both the emissivity and opacity of  $\nu_e$ 's and  $\bar{\nu}_e$ 's when the density is large enough, i.e., for rest mass density  $\rho \gtrsim 10^{13} \text{ g cm}^{-3}$ . The weak magnetism effect instead makes electron antineutrino's interactions less frequent, in particular when they have large energies, and remains relevant in regions at lower densities as well, including the ones where  $\bar{\nu}_e$  typically decouples from matter.

The paper is structured as follows: in Sec. II we present a general overview about the formalism of the collision integral for neutrino transport, as well as the physical content of the library in terms of reactions and microphysics

effects implemented and of the strategy followed to reconstruct the neutrino distribution functions. In Sec. III, we elaborate on how we extract representative thermodynamic conditions from a BNS merger simulation to evaluate neutrino reactions. Then, in Secs. IV and V we discuss the results obtained for neutrino emissivities, opacities, and surfaces in the postprocessing analysis, separately for the energy-dependent and energy-integrated cases. We also discuss the numerical performance of BNS\_NURATES in Sec. VI. Finally, we summarize the work and draw our conclusions in Sec. VII. Appendixes A to D are dedicated to the elucidation of technical details and the presentation of additional results.

## II. METHODS

This section summarizes and elaborates on the formalism and equations underlying the framework in which the BNS\_NURATES library has been developed. In the following, Greek (italic) letters run over spacetime (space) indexes. However, the notation  $A_x$  for some generic quantity  $A$  indicates dependence on the neutrino species ( $x \in \{\nu_e, \bar{\nu}_e, \nu_x, \bar{\nu}_x\}$ ), and any ambiguity is resolved in the text. We use  $\nu_x$  ( $\bar{\nu}_x$ ) as a generic notation for indicating either  $\nu_\mu$  ( $\bar{\nu}_\mu$ ) or  $\nu_\tau$  ( $\bar{\nu}_\tau$ ) neutrinos without distinction, as there are for now no interactions in our library yielding different rates for these two flavors. In some expressions, the symbol  $\nu$  stands for a neutrino of any species. We also adopt the convention to set the Boltzmann constant  $k_B = 1$ , so that temperatures are expressed in units of energy throughout.

### A. Collision integral and stimulated absorption

The transport of neutrinos is regulated by the interactions with the background matter field (hereafter fluid) and classically described by the Boltzmann equation for the neutrino distribution functions  $f_x(x^\mu, p^\mu)$ <sup>1</sup>:

$$p^\alpha \left[ \frac{\partial f_x}{\partial x^\alpha} + \Gamma_{\alpha\gamma}^i p^\gamma \frac{\partial f_x}{\partial p^i} \right] = (-p^\mu u_\mu) B_x(x^\mu, p^\mu, f_x), \quad (1)$$

where  $x^\mu$ ,  $u^\mu$ , and  $p^\mu$  are the spacetime coordinates, the fluid four-velocity, and the neutrino four-momentum in the laboratory frame, respectively. The four-momentum satisfies  $p^\mu p_\mu = 0$ , i.e., we consider massless neutrinos. In Eq. (1),  $\Gamma_{\alpha\gamma}^i$  are the Christoffel symbols of the background spacetime. We can decompose the four-momentum  $p^\alpha$  as

$$p^\alpha = k(u^\alpha + l^\alpha), \quad (2)$$

where  $k = -p^\mu x_\mu$  is the neutrino energy measured in the fluid frame and  $l^\alpha$  is a unit four-vector orthogonal to  $u^\alpha$ , encoding the angular dependence of the neutrino momenta (note that  $l_\alpha l^\alpha = l^2 = 1$  and  $u_\alpha l^\alpha = 0$ ). The angular dependence can also be expressed in terms of the angular variables  $\Omega = \{\theta, \phi\}$ , defined by the direction of propagation of neutrinos in the frame comoving with the fluid. In the following, we will omit the dependence on  $x^\mu$  for simplicity and specify the one on  $p^\mu$  in terms of  $(k, \Omega)$ . On the right-hand side of Eq. (1),  $B_x \equiv (df_x/d\tau)_{\text{coll}}$  is the collision integral (defined in terms of the fluid proper time,  $\tau$ ) which accounts for the neutrino interactions<sup>2</sup>:

$$\begin{aligned} B_x(k, \Omega, f_x) = & \\ & (1 - f_x) j_{\beta,x}(k) - f_x c \lambda_{\beta,x}^{-1}(k) \\ & + (1 - f_x) \int dk' \frac{k'^2}{(hc)^3} \int d\Omega' (1 - \bar{f}'_x) R_x^{\text{pro}}(k, k', \omega) - f_x \int dk' \frac{k'^2}{(hc)^3} \int d\Omega' \bar{f}'_x R_x^{\text{ann}}(k, k', \omega) \\ & + (1 - f_x) \int dk' \frac{k'^2}{(hc)^3} \int d\Omega' f'_x R_x^{\text{in}}(k, k', \omega) - f_x \int dk' \frac{k'^2}{(hc)^3} \int d\Omega' (1 - f'_x) R_x^{\text{out}}(k, k', \omega), \end{aligned} \quad (3)$$

where  $\bar{f}_x = \bar{f}_x(k, \Omega)$  is the distribution function of the antiparticle relative to the (anti)neutrino of flavor  $x$ . The primed notation for  $f'$  and  $\bar{f}'$  indicates a dependence on the integration variables  $(k', \Omega')$ . By inspecting the different terms that appear on the right-hand side of

Eq. (3), we can identify the contribution to the collision integral of different classes of reactions. The first row accounts for semileptonic charged-current processes, hereafter  $\beta$  processes, where a single neutrino takes part to the interaction. The second row describes reactions involving the emission or absorption of  $\nu\bar{\nu}$  pairs, quantified by the production and annihilation kernels,  $R_x^{\text{pro}}$  and  $R_x^{\text{ann}}$ , summed over the different interactions which fall within this class. Finally, the third row indicates the contribution of neutrino scattering reactions in terms of the  $R_x^{\text{in}}$  and  $R_x^{\text{out}}$  kernels. The kernels depend on the energies of both (anti)neutrinos taking part in the interaction and on the angle between their propagation directions, which

<sup>1</sup> In this section, several quantities such as  $p^\mu$  pertain to a given neutrino species, i.e.,  $p^\mu$  should be denoted as  $p_x^\mu$ . We employ the former notation in the interest of readability.

<sup>2</sup> Hereafter, it is understood that integrals over the energy range from 0 to  $+\infty$ , while integrals over angular dependence span the whole two-sphere.

we denote as  $\omega$ . The latter can be expressed in terms of the angular variables of the individual particles as

$$\omega = \cos \theta \cos \theta' + \sin \theta \sin \theta' \cos(\phi - \phi'). \quad (4)$$

We rewrite Eq. (3) by grouping together the positive and contributions of all reactions, including the scattering processes:

$$B_x(k, \Omega, f_x) = (1 - f_x(k, \Omega)) \left\{ \sum_l j_{l,x}(k, \Omega) \right\} - f_x(k, \Omega) \left\{ \sum_l c \lambda_{l,x}^{-1}(k, \Omega) \right\}, \quad (5)$$

where the index  $l$  runs over all reactions. This notation makes explicit how each process contributes to the production and removal of neutrinos and is chosen to facilitate the comparison between the different reactions. In the first term, the spectral emissivity,  $j_{l,x}$ , once integrated over the phase space, provides the number of neutrinos of flavor  $x$  and four-momentum  $(k, \Omega)$  that are produced per unit time by the  $l$ th reaction. This is weighted by the Pauli blocking factor of the final state,  $(1 - f_x)$ . Similarly, the spectral absorptivity  $c \lambda_{l,x}^{-1}$  (or inverse mean free path  $\lambda_{l,x}^{-1}$ ) quantifies the removal of neutrinos of given species and momentum per unit time, and is weighted by the neutrino occupation number  $f_x$ . We do not report explicitly the expression of  $j_{l,x}$  and  $c \lambda_{l,x}^{-1}$  for each process as they can be easily identified in Eq. (3) as the terms that multiply  $(1 - f_x)$  and  $f_x$ , respectively, depending on the reaction class.

Finally, Eq. (5) can also be rewritten in the following way:

$$B_x(k, \Omega, f_x) = \sum_l j_{l,x}(k, \Omega) - f_x(k, \Omega) \sum_l K_{l,x}(k, \Omega), \quad (6)$$

where  $K_{l,x} \equiv j_{l,x} + c \lambda_{l,x}^{-1}$  is the stimulated (spectral) absorptivity. This formalism will come in handy when discussing the source term of a gray M1 transport scheme in Sec. II C. The spectral inverse mean free paths presented in Sec. IV follow the notation appearing in Eq. (5).

## B. Neutrino reactions

The actual form of  $j_{l,x}$  and  $\lambda_{l,x}^{-1}$  depends on the neutrino-matter reaction under consideration. The set of reactions that are currently included in BNS\_NURATES is summarized in Table I. We distinguish between interactions involving a single neutrino and those involving two (anti)neutrinos among the initial and final states. In the former case, spectral emissivities and absorptivities are given by closed-form expressions, as one can integrate over the phase spaces of all the other particles involved

by assuming them to be in LTE conditions.  $\beta$  processes fall within this category. In the second case, we describe neutrino interactions in terms of the corresponding reaction kernels since the spectral emissivities and absorptivities specifically depend on the distribution function prescribed for the other (anti)neutrino participating in the reaction. This category includes pair and scattering processes. For such interactions, we expand the reaction kernels in a Legendre series, such that

$$R_{l,x}^{(\text{pro})}(\text{in})(k, k', \omega) = \sum_{m=0}^{+\infty} R_{l,x}^{(\text{pro})}(\text{in})^m(k, k') P_m(\omega), \quad (7)$$

where  $P_m(\omega)$  is the Legendre polynomial of order  $m$  and  $R_{l,x}^{(\text{pro})}(\text{in})^m$  is the  $m$ th coefficient of the expansion. For the evaluation of spectral emissivities and absorptivities, we truncate the expansion at  $m = 0$ . As a consequence,  $j_{l,x}$  and  $\lambda_{l,x}^{-1}$  do not have any angular dependence in the current version of BNS\_NURATES. The implementation of angular dependent interactions is left as a future enhancement of the library.

Hereafter we briefly discuss the implementation of the various reactions included in BNS\_NURATES, while we leave the presentation of the explicit formulas to Appendix A.

*a.  $\beta$  processes.*  $\beta$  processes are interactions in which a single neutrino induces a  $n \leftrightarrow p$  conversion by coupling with the corresponding lepton. They include electron and positron captures on nucleons, nucleon decays and the corresponding inverse reactions. We implement bare emissivities resulting from electron and positron captures following Ref. [70] (see also [77]), assuming nonrelativistic nucleons and zero momentum transfer; while the ones of neutron and proton decays are taken from Ref. [65] and derived under the same assumptions. To enhance the realism of the calculations, BNS\_NURATES implements weak magnetism and in-medium effects for  $\beta$  processes. The weak magnetism effect is introduced to compensate for the fact that the Pauli-tensor term of the nucleonic current is neglected when evaluating the matrix element of the reaction. It is applied as an energy-dependent multiplicative factor to the bare  $j_{\beta,x}$ , including also recoil and phase-space corrections, as discussed in Ref. [71]. For simplicity's sake, in the rest of the manuscript we will indicate the combination of these effects simply as weak magnetism. In-medium (or mean field) effects instead account for the modification of bare rates induced by the interactions between nucleons in the medium. The modification is stronger at higher densities, as the interaction potential energy is on average larger. In a relativistic mean field (RMF) formalism, this effect is introduced by replacing the bare nucleon mass with an effective one ( $m_i \rightarrow m_i^*$ ,  $i = n, p$ ) and by adding to the total single-particle energy the contribution of an interaction potential  $U_i$ . Clearly, this is an equation of state (EOS)-dependent effect. The way in which the effective mass difference,  $\Delta m^* \equiv m_n^* - m_p^*$ , and the interaction potential difference,  $\Delta U \equiv U_n - U_p$ , modify the standard ex-

$\beta$ processes [65, 70–72]	$p + e^- \leftrightarrow n + \nu_e$ $n + e^+ \leftrightarrow p + \bar{\nu}_e$
Electron-positron annihilation [70, 73]	$p \leftrightarrow e^+ + n + \nu_e$ $n \leftrightarrow e^- + p + \bar{\nu}_e$
Nucleon-nucleon bremsstrahlung [74, 75]	$e^- + e^+ \leftrightarrow \nu + \bar{\nu}$
Isoenergetic scattering off nucleons [70, 71]	$N + N \leftrightarrow N + N + \nu + \bar{\nu}$
Inelastic scattering off electrons and positrons [70, 76]	$N + \nu \rightarrow N + \nu$
	$e^\pm + \nu \rightarrow e^\pm + \nu$

TABLE I. Reactions included in BNS\_NURATES

pression of  $j_{\beta,x}$  has been discussed, e.g., in Refs. [65, 72]. The spectral absorptivity,  $c\lambda_{\beta,x}^{-1}$ , is obtained from the emissivity via detailed balance, i.e.,

$$c\lambda_x^{-1}(k) = j_x(k) e^{(k-\mu_x)/T}, \quad (8)$$

where  $T$  is the fluid temperature and  $\mu_{\nu_e} = -\mu_{\bar{\nu}_e} = \mu_p - \mu_n + \mu_e$  is the electron (anti)neutrino chemical potential at equilibrium, obtained from the relativistic chemical potentials of neutrons ( $\mu_n$ ), protons ( $\mu_p$ ), and electrons ( $\mu_e$ ).

*b. Pair processes.* We account for the production and absorption of  $\nu\bar{\nu}$  pairs via the electron-positron annihilation and the nucleon-nucleon bremsstrahlung (hereafter NN bremsstrahlung) and the corresponding inverse reactions. For each of the two interactions, the production and annihilation kernels are connected through the detailed balance relation:

$$R_{l,x}^{\text{ann}}(k, k', \omega) = e^{(k+k')/T} R_{l,x}^{\text{pro}}(k, k', \omega). \quad (9)$$

The kernel formulas for pair annihilation have been taken from Refs. [70, 73], while the ones for NN bremsstrahlung from Ref. [74], including the possibility for the latter to account for in-medium modifications of the kernel according to Ref. [75].

*c. Scattering processes.* We consider scattering reactions of neutrinos off both nucleons and  $e^\pm$ . In this case as well, each of the *in* and *out* scattering kernels are related through detailed balance:

$$R_{l,x}^{\text{out}}(k, k', \omega) = e^{(E_t - E'_t)/T} R_{l,x}^{\text{in}}(k, k', \omega), \quad (10)$$

where  $(E_t - E'_t)$  is the energy transferred to the target particle in the reaction. For conditions relevant to BNS mergers, the scattering off nucleons can be considered as quasielastic, i.e., the recoil is small due to the large mass of the targets compared with the typical neutrino energies, so that  $R_{\text{iso},x}^{\text{in}} = R_{\text{iso},x}^{\text{out}} \equiv R_{\text{iso},x}$ . The quasielastic (or isoenergetic) kernels follow Ref. [70] (or equivalently [77]) and account for phase-space, recoil and weak magnetism effects for neutral-current reactions from Ref. [71]. In this case as well, we will refer to the combination of these effects simply as weak magnetism. Note that for the evaluation of the isoenergetic spectral emissivities and absorptivities we expand the kernel considering only  $R_{\text{iso},x}^0$ , as mentioned before, but we include also  $R_{\text{iso},x}^1$  when computing the energy-integrated scattering opacities (see Sec. II C). In this latter case, before performing

the energy integration, it is also useful to apply the isoenergetic condition, i.e.,  $R_{\text{iso},x} = \bar{R}_{\text{iso},x}(k, \omega)\delta(k - k')$ , and write down its contribution to the collision integral as

$$B_x^{\text{iso}}(k) = \frac{k^2}{(hc)^3} \int d\Omega' \times [f_x(k, \Omega') - f_x(k, \Omega)] \bar{R}_{\text{iso},x}(k, \omega). \quad (11)$$

For the same physical conditions, the scattering off  $e^\pm$  is significantly inelastic and its scattering kernels are modeled as in Refs. [70, 76]. In the rest of the manuscript we will occasionally refer to the combination of  $\nu e^-$  and  $\nu e^+$  scattering reactions as (inelastic) neutrino-electron/positron scattering (NEPS).

### C. Energy-integrated emissivities and opacities

Following Ref. [78], the energy-dependent source terms for the radiation field equations in the moment-based transport formalism truncated to second order can be written (in the local rest frame of the fluid) as

$$S_{(k),x}^\alpha(k) = \frac{k^3}{(hc)^3} \int d\Omega B_x(k, \Omega, f_x)(u^\alpha + l^\alpha). \quad (12)$$

The energy-integrated version of Eq. (12) is defined in Eq. (5) of Ref. [48] and reads

$$S_x^\alpha \equiv \int dk S_{(k),x}^\alpha(k) = (\eta_x - \kappa'_{a,x} J_x) u^\alpha - (\kappa''_{a,x} + \kappa_{s,x}) H_x^\alpha, \quad (13)$$

where  $\eta_x$  is the gray neutrino emissivity,  $\kappa'_{a,x}$  and  $\kappa''_{a,x}$  are the two gray absorption opacities and  $\kappa_s$  is the gray scattering opacity. Note that  $\kappa'_a$  and  $\kappa''_a$  are in principle different from each other.  $J_x$  and  $H_x^\alpha$  are, respectively, the zeroth and first gray radiation energy moments, namely the neutrino energy density and the neutrino energy flux, i.e.,

$$J_x = \frac{1}{(hc)^3} \int dk k^3 \int d\Omega f_x(k, \Omega), \quad (14)$$

$$H_x^\alpha = \frac{1}{(hc)^3} \int dk k^3 \int d\Omega f_x(k, \Omega) l^\alpha. \quad (15)$$

Often, gray transport schemes involve scalar equations for the evolution of the neutrino number moments as well

(see, e.g., [47, 79], in which gray two-moment neutrino transports are employed in CCSN simulations). In this case, the zeroth-order moment is the neutrino number density,  $n_x$ , defined as

$$n_x = \frac{1}{(hc)^3} \int dk k^2 \int d\Omega f_x(k, \Omega). \quad (16)$$

These equations feature source terms of the form

$$\tilde{S}_x \equiv \int dk \tilde{S}_{(k),x}(k) = \tilde{\eta}_x - \tilde{\kappa}_{a,x} n_x, \quad (17)$$

with corresponding emissivities and absorption opacities,  $\tilde{\eta}_x$  and  $\tilde{\kappa}_{a,x}$ . Equation (17) represents the energy-integrated version of

$$\tilde{S}_{(k),x}(k) = \frac{k^2}{(hc)^3} \int d\Omega B_x(k, \Omega). \quad (18)$$

In order to evaluate the different coefficients in the moment expansion of the source terms, for each reaction we plug the corresponding collision integral into Eqs. (12) and (18), and we integrate over  $k$ . We then compare the outcome of this procedure with Eqs. (13) and (17), respectively, and map the different terms according to the order of the neutrino moments. In doing that, we find that the integrand defining  $\kappa''_{a,x}$  contains the sum of the stimulated spectral absorptivities. For the matter of coherence, when we map the terms proportional to  $u^\alpha$  in Eq. (13), we define also  $\kappa'_a$  in terms of  $K_{l,x}$ , with  $\eta$  that is consequently specified in terms of the unblocked spectral emissivities. In this way, it is possible to discuss the conditions under which  $\kappa'_a = \kappa''_a \equiv \kappa_a$ . In particular, this is realized when the angular integrations can be factored out from the ones over energy, so that the former either become trivial or cancel out in the computation of the gray averages. In order for this to happen, we truncate all the Legendre expansions of the inelastic kernels at the monopole contribution (see Sec. II B), so that spectral emissivities and absorptivities do not depend on angular variables. Furthermore, we consider neutrino distribution functions separable in their energy and angular dependence, i.e.,  $f_x(k, \Omega) = g_x(k) h_x(\Omega)$ , requiring that their angular part satisfies the relation  $\int d\Omega h_x(\Omega) = 4\pi$  (see Sec. II D). In this way, all the angular integrations can be carried out analytically, and gray emissivities and absorption opacities can be obtained from the spectral ones in the following way:

$$\tilde{\eta}_x = \frac{4\pi}{(hc)^3} \int dk k^2 \sum_{l'} j_{l',x}(k), \quad (19)$$

$$\eta_x = \frac{4\pi}{(hc)^3} \int dk k^3 \sum_{l'} j_{l',x}(k), \quad (20)$$

$$\tilde{\kappa}_{a,x} = \frac{4\pi}{c(hc)^3 n_x} \int dk k^2 g_x(k) \sum_{l'} K_{l',x}, \quad (21)$$

$$\kappa_{a,x} = \frac{4\pi}{c(hc)^3 J_x} \int dk k^3 g_x(k) \sum_{l'} K_{l',x}, \quad (22)$$

The sum over  $l'$  runs over all inelastic reactions, i.e., all the reactions implemented in the library except for the isoenergetic scattering off nucleons, which follows a different paradigm. In fact, its contributions cancel out with each other at the lowest order of the source terms' expansion, being an isoenergetic process. As a consequence, it does not contribute to Eq. (17). In fact, it only enters in Eq. (13) with a coefficient,  $\kappa_{s,x}$ , which is proportional to the neutrino energy flux. Starting from the collision integral in Eq. (11), one obtains <sup>3</sup>

$$\kappa_{s,x} = \frac{(4\pi)^2}{c(hc)^6 J_x} \int dk k^5 g_x(k) \times \left[ \tilde{R}_{\text{iso},x}^0(k) - \frac{\tilde{R}_{\text{iso},x}^1(k)}{3} \right]. \quad (23)$$

Because of the different nature of the interaction, this coefficient is distinguished from  $\kappa''_{a,x}$ . On the other hand, the cancellation does not occur in the case of inelastic scattering reactions. Therefore, we consider the scattering off  $e^\pm$  as equivalent to a neutrino emission/absorption process, contributing to  $\eta_x$  ( $\tilde{\eta}_x$ ) and  $\kappa_{a,x}$  ( $\tilde{\kappa}_{a,x}$ ) together with the other inelastic reactions. Notice that the evaluation of Eqs. (19)-(23) requires us to perform a one-dimensional numerical integration over the neutrino energy in the case of  $\beta$  processes and isoenergetic scattering, and a two-dimensional integration over the energies of the two (anti)neutrinos participating in the interaction for the other classes of reactions. The way in the numerical integrations are performed in the library is detailed in Appendix B.

#### D. Reconstruction of the neutrino distribution functions

This section describes the procedure employed by BNS\_NURATES to reconstruct the neutrino distribution function in the context of a gray transport scheme. We assume that the functional form of  $f_x$  is separable, and we isolate its energy and angular dependent parts, i.e.,  $f_x(k, \Omega) = g_x(k) h_x(\Omega)$ . We write the energy-dependent part  $g_x$  as a linear combination of a trapped contribution and a free-streaming one, labeled using the subscripts  $t$  and  $f$ , respectively:

$$g_x(k) = w_{t,x} g_{t,x}(k) + w_{f,x} g_{f,x}(k), \quad (24)$$

with constant weights  $w_{t,x}$  and  $w_{f,x}$ . For the trapped contribution we adopt a Fermi-Dirac distribution with temperature and degeneracy parameter denoted as  $T_{t,x}$  and  $\eta_{t,x}$ :

$$g_{t,x}(k) = \left[ e^{(k/T_{t,x} - \eta_{t,x})} + 1 \right]^{-1}, \quad (25)$$

<sup>3</sup> The simplified form of the collision integral allows us to retain the first-order term of the Legendre expansion of the kernel without introducing any nonanalytical angular integration.

while the free-streaming one is modeled as a generalized Maxwell-Boltzmann distribution with temperature  $T_{f,x}$ , pinching parameter  $c_f$ , and normalization factor  $\beta_{f,x}$ :

$$g_{f,x}(k) = \beta_{f,x} k^{c_{f,x}} e^{-k/T_{f,x}}. \quad (26)$$

We fix  $c_f = 0.6$  for all neutrino species following the fits presented in Ref. [80] in the context of CCSNe. No prescription is made regarding the functional form of the angular part of the distribution function, we only require that it satisfies  $\int d\Omega h_x(\Omega) = 4\pi$ . This relation is fulfilled exactly both in the trapped and free-streaming regimes, where  $h(\Omega)$  is either constant or forward peaked along the direction of propagation. It is only approximately fulfilled in a generic situation in between the two extremes. This simplification allows us to avoid dealing with complex and computationally expensive quadratures over the angular variables in the computation of emissivities and opacities.

In the following we detail how the parameters appearing in the distribution function are set. Two options are considered: reconstruction from M1 quantities and equilibrium with the fluid.

*a. Reconstruction from gray M1 neutrino quantities* The Eddington factor is used to weight the trapped and free-streaming parts in Eq. (24) in the same way as in the Minerbo closure [81], i.e.,  $w_{f,x} = (3\chi_x - 1)/2$  and  $w_{t,x} = 3(1 - \chi_x)/2$ . To reconstruct the parameters entering the trapped component, we require it to satisfy Eqs. (16) and (14), resulting in

$$n_x = \frac{4\pi}{(hc)^3} T_{t,x}^3 F_2(\eta_{t,x}), \quad (27)$$

$$J_x = \frac{4\pi}{(hc)^3} T_{t,x}^4 F_3(\eta_{t,x}), \quad (28)$$

where complete Fermi-Dirac integrals of order  $p$  are denoted as  $F_p$ . The ratio between Eqs. (28) and (27) gives  $T_{t,x}$  as a function of  $\eta_{t,x}$ :

$$T_{t,x} = \frac{J_x}{n_x} \frac{F_2(\eta_{t,x})}{F_3(\eta_{t,x})}. \quad (29)$$

Plugging Eq. (29) into Eq. (27), one gets the relation

$$1 = \frac{4\pi}{(hc)^3} \frac{J_x^3}{n_x^4} \frac{[F_2(\eta_{t,x})]^4}{[F_3(\eta_{t,x})]^3}, \quad (30)$$

which can be inverted to find  $\eta_{t,x}$ . We approximate the inverse of  $\tilde{F}(\eta) = [F_2(\eta)]^4 / [F_3(\eta)]^3$  as a piecewise high-order rational function split into three different intervals, achieving an accuracy with a relative error of at most  $10^{-2}$  over the values of interest, i.e.,  $\eta_t \in [-5, 5]$ . Once  $\eta_{t,x}$  is known, Eq. (29) returns the value of  $T_{t,x}$ . We evaluate Fermi-Dirac integrals using the fast and accurate approximated formulas provided by Ref. [82].

In the free-streaming regime, the same line of reasoning results in the zeroth number and energy moments being

written in terms of the Gamma function  $\Gamma(x)$ :

$$n_x = \frac{4\pi\beta_{f,x}}{(hc)^3} T_{f,x}^{c_f+3} \Gamma(c_f + 3), \quad (31)$$

$$J_x = \frac{4\pi\beta_{f,x}}{(hc)^3} T_{f,x}^{c_f+4} \Gamma(c_f + 4). \quad (32)$$

By applying the identity  $x = \Gamma(x + 1)/\Gamma(x)$  to the ratio between Eqs. (32) and (31), the value of the temperature is reconstructed as

$$T_{f,x} = \frac{J_x}{n_x(c_f + 3)}. \quad (33)$$

Then, by combining Eqs. (31) and (33), we recover the value of  $\beta_{f,x}$  as well:

$$\beta_{f,x} = \frac{(hc)^3 n_x}{4\pi \Gamma(c_f + 3)} \frac{1}{T_{f,x}^{c_f+3}}. \quad (34)$$

Note that although the parameters have been reconstructed separately for the trapped and free-streaming parts, the condition  $w_{t,x} + w_{f,x} = 1$  ensures that also the full  $g_x$  satisfies Eqs. (14) and (16). Moreover, the neutrino energy flux density  $H_x^\alpha$  is not required for the reconstruction, since we do not need to model explicitly the angular part of  $f_x$ .

*b. Equilibrium distribution function with optically thin correction* If we assume the distribution function to describe equilibrium with the fluid, we set  $w_{f,x} = 0$  and  $w_{t,x} = 1 \forall x$ . The distribution function is then a Fermi-Dirac function with parameters set by thermal and chemical equilibrium as

$$T_{t,x} = T, \quad (35)$$

$$\eta_{t,\nu_e} = \frac{\mu_p - \mu_n + \mu_e}{T}, \quad (36)$$

$$\eta_{t,\bar{\nu}_e} = -\eta_{t,\nu_e}, \quad (37)$$

$$\eta_{t,\nu_x} = 0. \quad (38)$$

The equilibrium assumption breaks down once neutrinos and matter decouple from each other. In order to account for it, one can correct the energy-integrated absorption and scattering opacities by the following multiplicative factor [47, 48]:

$$C_{\text{thin}} = \left( \frac{\varepsilon_x}{\varepsilon_{\text{eq},x}} \right)^2, \quad (39)$$

where  $\varepsilon_x \equiv J_x/n_x$  is the local average neutrino energy, as evolved by the gray M1 transport scheme, while  $\varepsilon_{\text{eq},x}$  is the one at thermodynamic equilibrium. This choice is motivated by the fact that the interactions taken into account have cross sections scaling as  $T^2$ . Equation (39) is close to  $\sim 1$  as long as the equilibrium assumption is justified, while in optically thin conditions it is able to approximately reproduce the opacities as obtained from the local neutrino quantities, as shown in Sec. VC.

### III. POSTPROCESSING STRATEGY

#### A. Simulation overview

We consider an equal mass BNS system with neutron star (NS) masses of  $\sim 1.298 M_\odot$ . We numerically evolve it through the inspiral, merger, and postmerger phases using the gray moment-based general-relativistic neutrino-radiation hydrodynamics code `THC_M1` [48, 83–85], which is based on the Einstein Toolkit [86, 87]. The relevant neutrino reactions used in this code and their implementation are detailed in Ref. [20]. While there is a good overlap with the reactions described in Sec. II B (with the notable exceptions of the scattering off electrons/positrons and nucleon decays), we stress that they differ substantially from the ones in `BNS_NURATES` in terms of accuracy and actual implementation. This is, however, not relevant for this work, since the simulation outcome will be only used to provide suitable fluid and radiation conditions to test the new library. Spacetime is consistently evolved by the `CTGAMMA` code [88, 89], which solves the Z4c formulation of Einstein’s field equations [90, 91].

We use the `CARPET` adaptive mesh refinement driver [92, 93], implementing the Berger–Olinger scheme with re-fluxing [94, 95]. In particular, the evolution grid employs seven levels of refinement and the spatial resolution is halved at each finer grid. The merging binary is simulated at a resolution for which the spacing of the finest grid is equal to  $\Delta x \approx 247$  m. Within such a scheme, during the inspiral, mass conservation is achieved with a typical relative accuracy of  $\sim 10^{-11}$  per iteration, on average positive. After merger, the relative variation per iteration increases ( $\sim 10^{-9}$ ), possibly also due to failures in the primitive variable reconstructions both in the dense and dilute portions of the computational domain. The total increase in mass is partially compensated by the ejecta leaving the computational domain once the ejection of matter from the system sets off.

To close the system of hydrodynamics equations and to provide the density-, temperature-, and composition-dependent quantities required by the gray neutrino transport, we adopt the Hempel and Schaffner-Bielich (Density Dependent 2) EOS [96, 97] (hereafter DD2 EOS). This is a rather stiff EOS that predicts a maximum non-rotating NS mass of  $2.42 M_\odot$  and a radius  $R_{1.4} = 13.2$  km for a nonrotating  $1.4 M_\odot$  NS. We employ this EOS since it generally provides long-lived merger remnants, especially in the case of light BNS systems.

To account for turbulent viscosity of magnetic origin, we employ the general-relativistic large-eddy simulation formalism [98, 99]. Within this formalism, turbulent viscosity is parametrized in terms of a density-dependent prescription for the characteristic length scale, which was calibrated using data from the high-resolution general-relativistic magnetohydrodynamics simulations of Refs. [24, 100, 101].

Irrotational,  $T \approx 0$ , neutrinoless weak-equilibrium ini-

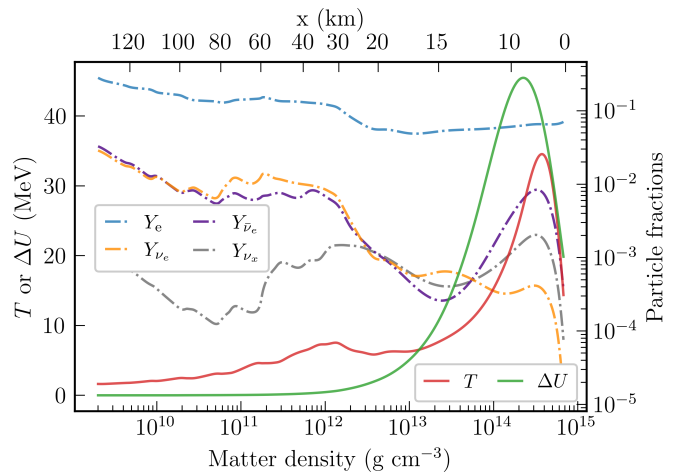


FIG. 1. Profiles of the matter temperature,  $\Delta U$ , electron fraction, and neutrino abundances as a function of the rest mass density as extracted from the simulation along the positive  $x$  axis.

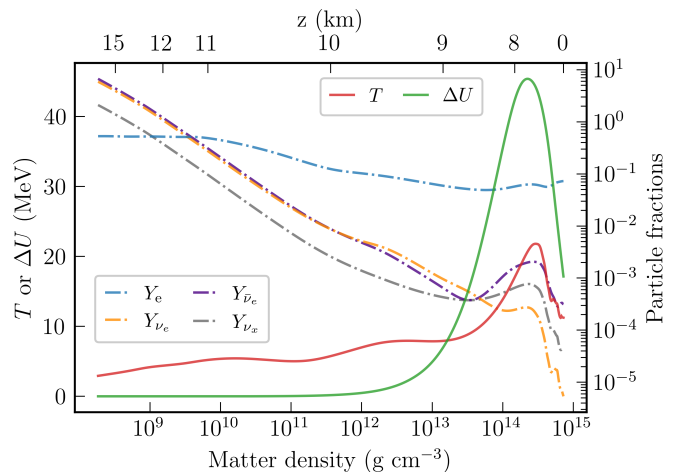


FIG. 2. Same as Fig. 1, but along the positive  $z$  axis.

tial data are constructed using the pseudospectral code `LORENE` [102], selecting an initial separation of 45 km.

#### B. Calculation of emissivity and opacity

To compute neutrino emissivities and opacities in conditions that are relevant for BNS mergers, we extract them from the simulation presented in Sec. III A, at  $t = 50$  ms after merger. At this point in the evolution, the remnant is approximately axisymmetric and it has reached a quasistationary state, further evolving on the longer cooling and viscous timescales. In our postprocessing procedure, we consider (i) single grid points, (ii) one-dimensional slices, as well as (iii) the whole three-dimensional computational domain.

In the first case, we define a set of reference rest mass densities,  $\{\rho_i\}$ , including a value close to the maximum

Name	$\rho$ [g cm <sup>-3</sup> ]	$T$ [MeV]	$Y_e$	$(Y_{\nu_e}, Y_{\bar{\nu}_e}, Y_{\nu_x})$ $(Z_{\nu_e}, Z_{\bar{\nu}_e}, Z_{\nu_x})$ [MeV] $(\chi_{\nu_e}, \chi_{\bar{\nu}_e}, \chi_{\nu_x})$	$\Delta U$ [MeV]	$(m_n^*, m_p^*)$ [10 <sup>2</sup> MeV]	$\hat{\mu}$ [MeV]	$\mu_e$ [MeV]
A	$6.90 \times 10^{14}$	12.39	0.07	$(0.09, 2.93, 0.54) \times 10^{-4}$ $(0.03, 1.29, 0.21) \times 10^{-2}$ (0.33, 0.33, 0.33)	$1.90 \times 10^1$	(2.81, 2.80)	$2.10 \times 10^2$	$1.87 \times 10^2$
B	$9.81 \times 10^{13}$	16.63	0.06	$(0.36, 2.21, 0.92) \times 10^{-3}$ $(0.18, 1.23, 0.48) \times 10^{-1}$ (0.33, 0.33, 0.33)	$3.48 \times 10^1$	(7.36, 7.35)	$9.90 \times 10^1$	$8.23 \times 10^1$
C	$9.87 \times 10^{12}$	8.74	0.06	$(0.82, 2.01, 0.84) \times 10^{-3}$ $(0.22, 0.57, 0.23) \times 10^{-1}$ (0.33, 0.33, 0.33)	4.98	(9.16, 9.15)	$4.11 \times 10^1$	$3.65 \times 10^1$
D	$1.00 \times 10^{12}$	6.61	0.11	$(0.72, 0.45, 0.15) \times 10^{-2}$ $(1.51, 0.93, 0.39) \times 10^{-1}$ (0.33, 0.33, 0.33)	0.47	(9.37, 9.36)	$1.76 \times 10^1$	$1.94 \times 10^1$
E	$1.00 \times 10^{11}$	3.60	0.14	$(10.92, 7.88, 0.29) \times 10^{-3}$ $(12.48, 10.21, 0.83) \times 10^{-2}$ (0.34, 0.37, 0.36)	$0.45 \times 10^{-1}$	(9.39, 9.38)	8.44	9.05
F	$1.01 \times 10^{10}$	2.17	0.19	$(12.56, 13.00, 0.36) \times 10^{-3}$ $(11.89, 15.56, 0.96) \times 10^{-2}$ (0.53, 0.57, 0.59)	$0.72 \times 10^{-3}$	(9.40, 9.38)	4.57	4.17

TABLE II. Properties of the representative grid points A–F extracted from the simulation at  $t = 50$  ms after merger.  $\rho$  represents the rest mass density,  $T$  the fluid temperature,  $Y_e$  the electron fraction,  $Y_x$ ,  $Z_x$ , and  $\chi_x$  (with  $x \in \{\nu_e, \bar{\nu}_e, \nu_x\}$ ) the neutrino number fractions, energy fractions and Eddington factors, respectively,  $\Delta U$  the neutron-to-proton RMF interaction potential difference,  $(m_n^*, m_p^*)$  the effective nucleon masses,  $\hat{\mu}$  the neutron-to-proton chemical potential difference, and  $\mu_e$  the electron chemical potential. Please note that here the chemical potentials are the relativistic ones, i.e., they include the rest mass contribution.

rest mass density inside the remnant (point A) and several other densities almost equally spaced in logarithmic space (points B–F). For each of them, we compute the volume-averaged density,  $\langle \rho_i \rangle$ , temperature,  $\langle T_i \rangle$ , and electron fraction,  $\langle Y_{e,i} \rangle$ , evaluated over all the cells with density  $\rho$  satisfying the condition  $|\rho - \rho_i|/\rho_i \leq 0.05$  and within an angular slice of width  $\Delta\theta \sim 20^\circ$  across the equatorial plane. After that, we search for the point inside the same region whose conditions are the closest to the averaged ones by minimizing the Euclidean distance with respect to  $(\log\langle \rho_i \rangle, \langle T_i \rangle, \langle Y_{e,i} \rangle)$ . This procedure ensures that the selected points are representative. Table II summarizes the conditions of the selected points and their most relevant properties.

For 1D slices, starting from the center of the computational domain, we consider all the cells along the positive  $x$  or  $z$  axis, for a fixed refinement level. In Figs. 1 and 2 we present the profiles of the temperature, the RMF potential energy shift,  $\Delta U$ <sup>4</sup>, and the relevant particle abundances as a function of the rest mass density along the positive  $x$  and  $z$  axis, respectively.

We instead consider the entire three-dimensional do-

main when we compute the position of the neutrino surfaces (see Sec. III C). In this case, the computational grid extends over the entire region covered by the coarsest refinement level and is defined in terms of spherical coordinates with a log-spaced radial mesh and equally spaced angular bins.

In all three cases, the data that we extract from the simulation are the thermodynamic conditions  $(\rho, T, Y_e)$  (necessary to call the EOS), as well as the neutrino quantities evolved by the M1 scheme, i.e.,  $n_x$ ,  $J_x$ , and the Eddington factor,  $\chi_x$ , for all the relevant neutrino species. We then employ the neutrino quantities to reconstruct the neutrino distribution functions, as detailed in Sec. II D. Once the conditions are set, we use the BNS\_NURATES library to compute both energy-dependent and energy-integrated emissivities and opacities for all neutrino species and for all the reactions presented in Sec. II B. Note that the simulation just considers three neutrino species, i.e.,  $\{\nu_e, \bar{\nu}_e, \nu_x\}$ , as the employed neutrino scheme does not involve any reaction that distinguishes between heavy-type neutrinos and antineutrinos. On the other hand, in BNS\_NURATES, the implementation of the inelastic neutrino scattering off  $e^\pm$  introduces that sort of distinction. Nonetheless, as the difference is only marginal, in Secs. IV and V we just present the results for  $\nu_x$  neutrinos.

<sup>4</sup> The EOS employed predicts  $\Delta m^* = \Delta m$  for any condition, therefore the information about RMF effects is completely encoded into the value of  $\Delta U$ .

### C. Neutrino surface calculations

The neutrino optical depth,  $\tau_x$ , quantifies the number of interactions experienced by diffusing neutrinos along a certain path. Denoting as  $P_B(\mathbf{x}; t)$  the set of all paths that reach the boundary of our computational domain at time  $t$  starting from the point  $\mathbf{x}$ , the optical depth can be defined as

$$\tau_x(\mathbf{x}; t) := \min_{\Gamma \in P_B(\mathbf{x}; t)} \int_{\Gamma} \lambda_x^{-1} ds. \quad (40)$$

We then define neutrino surfaces as the isosurfaces where  $\tau_x$  attains the value  $2/3$ . Energy-dependent inverse mean free paths result in energy-dependent optical depths and neutrino surfaces. Depending on the definition of  $\lambda_x^{-1}$  entering in Eq. (40), two types of optical depths are usually considered: the diffusion optical depth ( $\tau_{\text{diff},x}$ ) and the equilibration optical depth ( $\tau_{\text{eq},x}$ ). In the former case, one has that

$$\lambda_{\text{diff},x}^{-1} \equiv \sum_l \lambda_{l,x}^{-1}, \quad (41)$$

where the sum runs over all processes providing opacity, and the neutrino surfaces correspond to the last interaction surface for a neutrino moving from optically thick to optically thin regions. In the second case, one has instead that

$$\lambda_{\text{eq},x}^{-1} \equiv \sqrt{\left( \sum_{l'} \lambda_{l',x}^{-1} \right) \lambda_{\text{diff},x}^{-1}} \quad (42)$$

and the sum runs on inelastic processes only. In this case, the neutrino surfaces enclose the portion of the system in which neutrinos are in thermal contact with matter.

We consider a snapshot of the 3D computational domain as extracted from our simulation at  $t = 50$  ms after merger and we compute energy-dependent optical depths and neutrino surfaces using Eq. (40), relying on the algorithm depicted in Appendix C. The neutrino surfaces presented in Secs. IV B and IV C are isosurfaces of the equilibration optical depth,  $\tau_{\text{eq},x}$ .

## IV. RESULTS: ENERGY DEPENDENT RATES

### A. Reaction comparison

In Figs. 3 and 4 we show spectral emissivities (top panels) and inverse mean free paths (middle panels) for different reactions, as well as the neutrino distribution functions (bottom panels), under the thermodynamic conditions characterizing points A and B in Table II, respectively, and over the neutrino energy interval relevant for BNS merger conditions. We recall that point A was chosen as a representative point for the conditions in the densest part of the remnant. Solid lines were obtained

by using the reconstructed distribution functions, while dashed lines the equilibrium ones. The scattering off nucleons appears only in the middle panels since, due to its elastic nature, it does not affect the distribution of the neutrino energy but it still significantly contributes to the opacity of neutrinos. Indeed, it is the dominant contribution to the inverse mean free path in many regimes, especially at  $k \gtrsim 10$  MeV.

Inelastic neutrino interactions at points A and B are distinguished by a qualitative difference, associated with the relative importance of  $\beta$  processes for electron-type (anti)neutrinos. In the center of the remnant, the contribution of both (inverse) electron and positron captures and (inverse) nucleon decays, shown in red and purple lines respectively, are suppressed either by the high degeneracy of neutrons and electrons or by the paucity of positrons, depending on the direction in which the reactions proceed. Only absorptions on neutrons of highly energetic  $\nu_e$  ( $k_{\nu_e} \gtrsim 100$  MeV) are relevant, as they are able to produce electrons in the final state above the Fermi level ( $\mu_e \approx 190$  MeV). As a consequence, the neutrino dynamics in the center of the remnant is established by other reactions, similarly to what happens generally in the case of heavy-type neutrinos. For example, the (inverse) NN bremsstrahlung, associated with orange lines, is the most relevant process in terms of emission (absorption) of soft neutrinos of any flavor. Inelastic NEPS is also an important process for neutrinos in the center of the remnant (cyan lines). High-energy neutrinos have a larger probability to scatter off energetic electrons and excite them above the degeneracy level. Assuming that neutrino distribution functions are close to the equilibrium ones, as shown in the bottom panels, NEPS efficiently produces neutrinos in the final state with a broad energy spectrum. While for very soft neutrinos its contribution is always subdominant with respect to NN bremsstrahlung, it becomes very relevant for  $k \gtrsim 20$  MeV or even lower energies for  $\bar{\nu}_e$ .

Moving out from the center of the remnant, the density decreases and charged-current reactions are no longer inhibited. According to the left panel of Fig. 4, in the region where point B is located, electron captures and absorption on neutrons are the dominant reactions undergone by  $\nu_e$  neutrinos of any energy, once microphysics effects are accounted for (cf. solid red lines). Electron captures on protons retain an almost constant emissivity ( $j \sim 10^7 \text{ s}^{-1}$ ) until several tens of MeV, before dropping off as a consequence of the low occupation of highly energetic electrons above the Fermi level. At the same time, the mean free path associated with  $\nu_e$  absorptions on neutrons is well below the size of the remnant (a few  $\sim 10^6$  cm) for any neutrino energy. Other contributing processes for the electron neutrino dynamics are the scattering off nucleons and the (inverse) NN bremsstrahlung, with the latter that partially increases the overall emissivity and inverse mean free path for soft enough  $\nu_e$  ( $\sim 10\%$  increase for  $k \lesssim$  a few MeV). Other reactions are instead subdominant in these conditions, such as

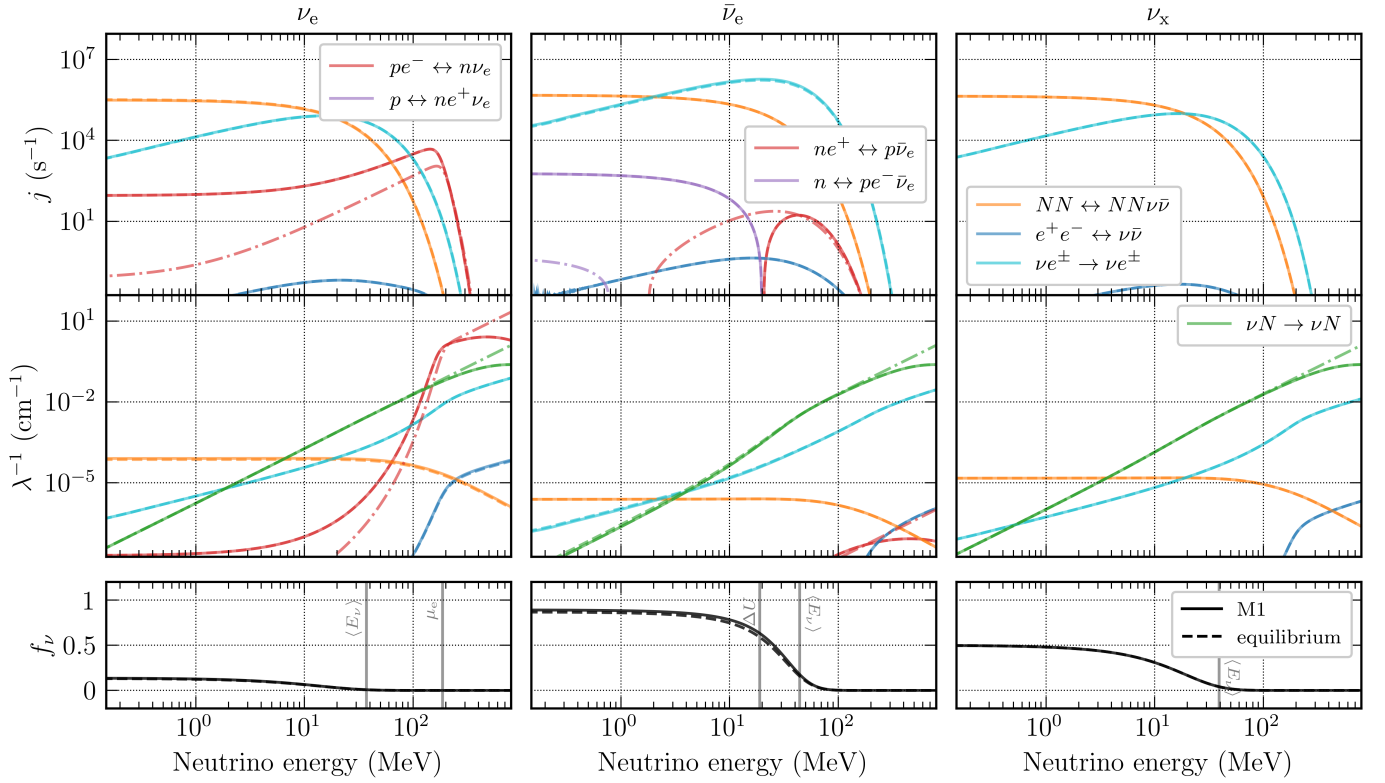


FIG. 3. Top (middle) row: spectral emissivity (inverse mean free path) for different reactions and for the thermodynamic conditions of point A in Table II. Bottom row: neutrino occupation number as a function of the neutrino energy, superimposed to some relevant energy scales. Left, center, and right panels refer to electron neutrinos, electron antineutrinos, and heavy-type neutrinos, respectively. Solid lines were obtained by using the reconstructed distribution functions, while dashed lines the equilibrium ones. In both cases,  $\beta$  processes account for weak magnetism and RMF effects and isoenergetic scattering reactions for weak magnetism. Red, purple, and green dot-dashed lines differ from solid ones for the absence of such effects.

(inverse)  $e^+e^-$  annihilations (blue lines), inhibited for any flavor by the electron degeneracy at high densities, and (inverse) proton decays, which turn out to be kinematically forbidden for any conditions considered in this study, particularly when considering the impact on its kinematics due to RMF effects. Speaking of such effects, the central panels of Fig. 4 highlight their importance when considering electron antineutrino interactions. Because of kinematics constraints, charged-current interactions are possible only below or above a given neutrino energy threshold. Under the assumption of zero-momentum transfer, the threshold energies for (inverse) positron captures and (inverse) neutron decays are separated by an energy gap of  $2m_e \sim 1$  MeV, whose position in the spectrum is ultimately determined by the average nucleon energy difference. Therefore, when RMF effects are taken into account, the values of the energy thresholds are modified from  $\Delta m \pm m_e$  to  $\Delta m^* + \Delta U \pm m_e$ . Since RMF effects are sizable for high enough densities (see Figs. 1 and 2), as in the case of point B, the kinematic thresholds are effectively shifted to higher energies ( $\Delta U \sim 35$  MeV). This confines  $e^+$  captures and absorptions on protons to be effective only for  $\bar{\nu}_e$  with  $k \gtrsim$  several tens of MeV. At the same time, the influence of

(inverse) neutron decays extends over a broader energy range and becomes significant for determining the behavior of soft electron antineutrinos. It is also interesting to notice how the contribution from  $\bar{\nu}_e e^\pm$  scattering helps to make the energy dependence of the total  $j_{\bar{\nu}_e}$  and  $\lambda_{\bar{\nu}_e}^{-1}$  smoother, by partially filling the void between the two energy thresholds due to electron antineutrinos not undergoing  $\beta$  processes (which is also an artifact of our approximated RMF treatment with respect to more sophisticated approaches, see [65]). In comparison to the electron neutrino case, once we combine together the contributions of the various processes, we find that  $j_{\bar{\nu}_e}$  is dominated by neutron decays for the production of soft particles, while it is suppressed by the lower occupation of positrons compared to electrons at higher energies ( $k \sim$  a few tens of MeV), where  $j_{\nu_e}$  instead peaks. Similarly, the total inelastic  $\lambda_{\bar{\nu}_e}^{-1}$  is typically smaller than the one of  $\nu_e$ , in particular for highly energetic neutrinos. The latter feature is a direct consequence of the partial Pauli blocking from neutrons, which is still relevant even if less important than for point A, and of the fact that at large enough energies  $\nu_e$  absorptions are no longer inhibited by the degeneracy of final-state electrons.

Because of the absence of  $\mu^\pm$  and  $\tau^\pm$  leptons in our

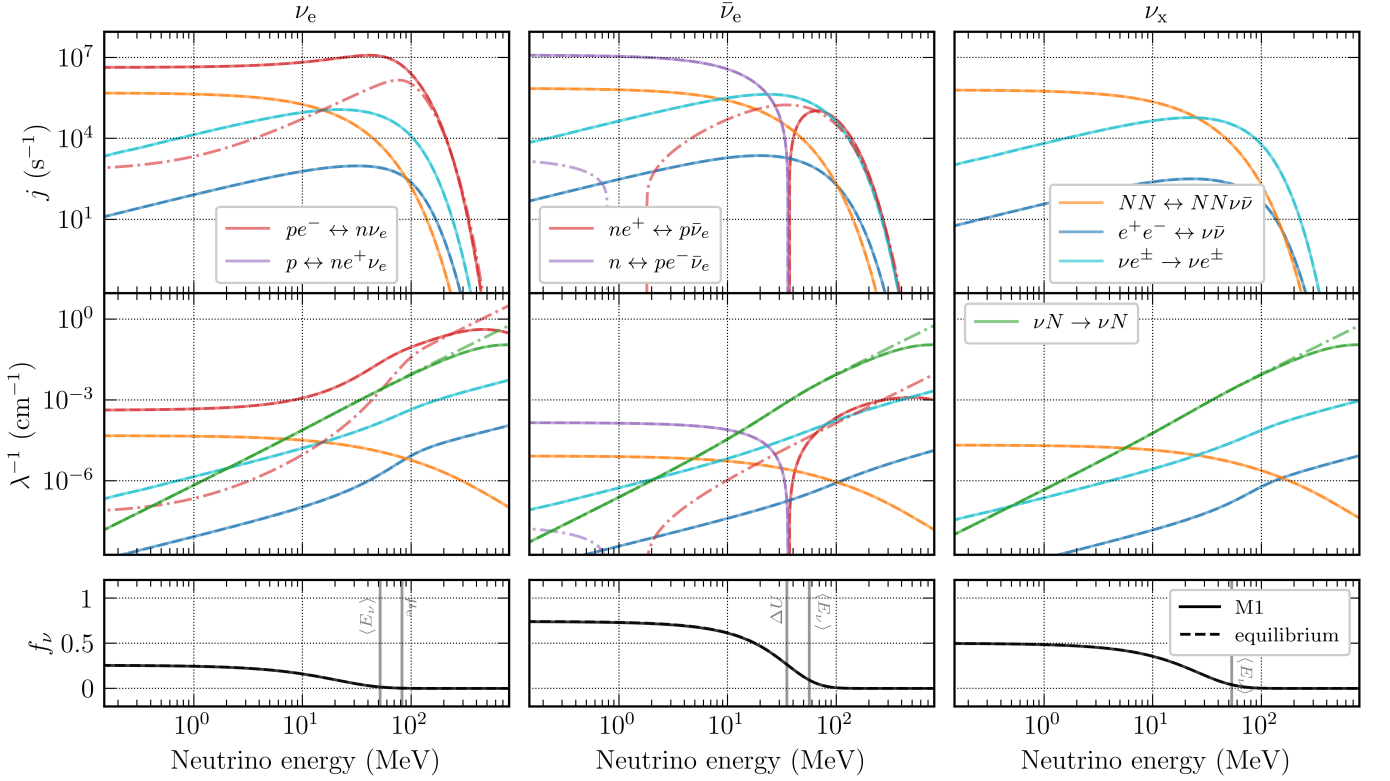


FIG. 4. Same as Fig. 3 but for thermodynamic point B in Table II.

description of the system,  $\nu_x$  production and removal rely on pair processes and inelastic scattering off  $e^\pm$ . Therefore, heavy-type neutrinos are typically created and destroyed at comparable or smaller rates than electron-flavored ones, especially where  $\beta$  processes are relevant. On the other hand, the contribution to the opacity of elastic scattering reactions off nucleons is similar with respect to the one seen for the other neutrino flavors. Focusing on inelastic processes, NN bremsstrahlung can efficiently convert nucleon energy into  $\nu_x \bar{\nu}_x$  pairs populating the softest part of the spectrum, and vice versa. For individual energies  $\lesssim 20$  MeV, in typical conditions inside the remnant, NN bremsstrahlung guarantees an emissivity of at least  $\sim 10^5 \text{ s}^{-1}$  and a mean free path that is smaller than the typical remnant size ( $\lambda_{\nu_x}^{-1} \gtrsim 10^{-5} \text{ cm}^{-1}$ ). The contribution of  $\nu_x e^\pm$  scattering is qualitatively similar to the case of electron (anti)neutrinos, but the impact on the total  $j_{\nu_x}$  and  $\lambda_{\nu_x}^{-1}$  is more significant as there are no charged-current reactions. In fact, it extends the upper tail of  $j_{\nu_x}$  to slightly higher energies and, most importantly, it significantly increases the equilibration inverse mean free path, see Eq. (42), ultimately affecting the decoupling conditions of  $\nu_x$  neutrinos from matter, as discussed in more detail in Sec. IV B. This reaction hierarchy for heavy-type neutrinos is qualitatively similar to the one found by Ref. [103] for similar conditions in CCSNe.

Emissivities and inverse mean free paths tend to decrease for all reactions once density and temperature be-

come smaller. Since the transition between the high and the low density regime is gradual, we avoid commenting points at intermediate densities (C–E), but we include the relative figures in Appendix D. A detailed reaction comparison is repeated in Fig. 5 only for the conditions extracted at point F in Table II, in order to understand how the different processes behave away from the densest parts of the remnant, where neutrinos stream freely. Based on the simulation outcome, the neutrino number densities in this region are  $\sim 2 - 4$  orders of magnitude smaller compared to the ones at point B. Also the average neutrino energies are smaller ( $\sim 10$  MeV for  $\nu_e$  and  $\bar{\nu}_e$  and  $\sim 20$  MeV for  $\nu_x$ , compared to  $\sim 50$  MeV for all the species at point B). Electron captures remain the most effective channel for emitting new  $\nu_e$  neutrinos, but the emissivity is  $\sim 6$  orders of magnitude smaller than the one at point B for  $k \lesssim 10$  MeV. The difference is even more pronounced above that, as the emitted spectrum is now cut off at lower energies, due to electrons being on average less energetic ( $\mu_e \approx 4$  MeV). On the opacity side, the upper bound on the total  $\lambda_{\nu_e}^{-1}$  is still determined mainly by  $\nu_e n$  absorptions, with a secondary contribution coming from  $\nu_e N$  scattering for  $k \gtrsim 1$  MeV. Differently from what was discussed for points at higher densities, in these conditions the NN bremsstrahlung is suppressed for any neutrino flavor, even for small energies, as it becomes particularly inefficient at low densities due to its pair nature. In the case of electron antineutrinos, we observe how the energy thresholds of  $\beta$  processes have rolled back towards

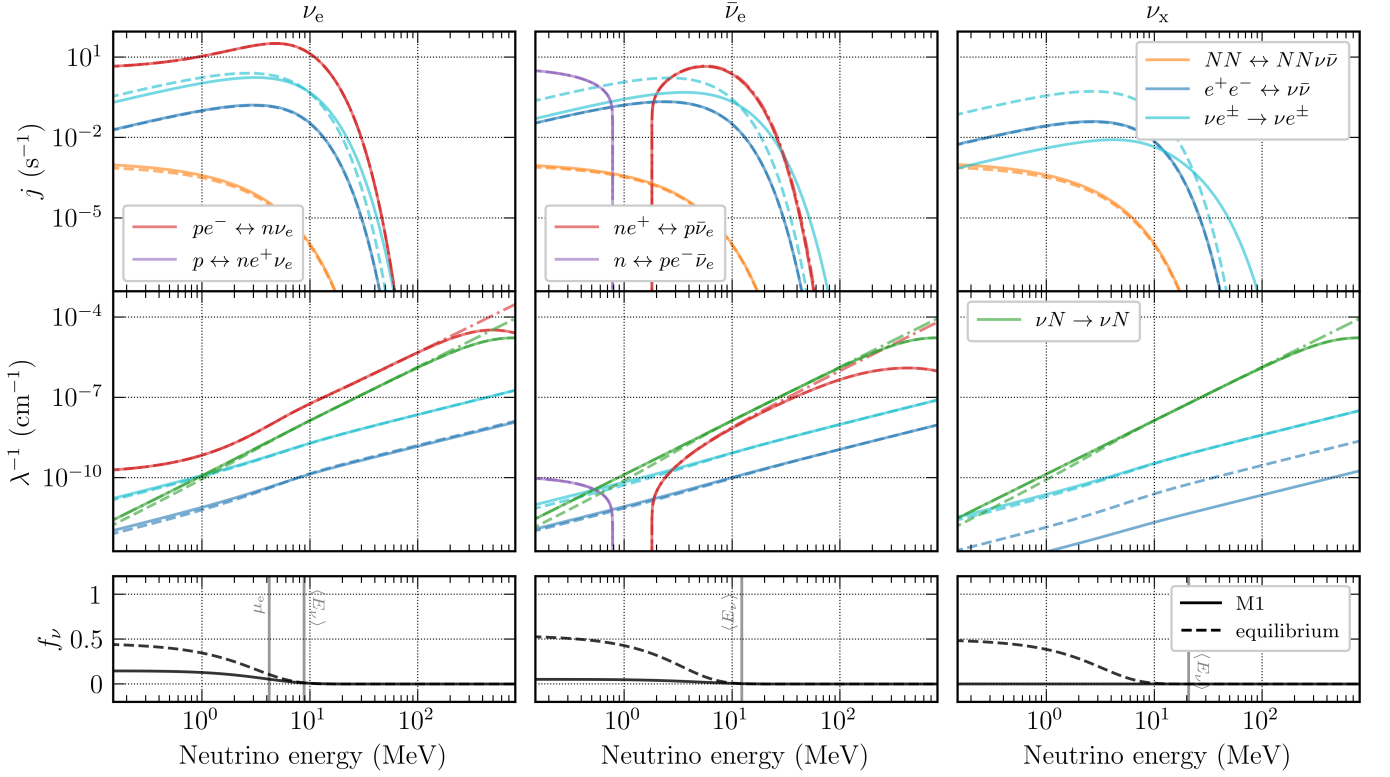


FIG. 5. Same as Fig. 3 but for thermodynamic point F in Table II.

energies of around  $\sim 1$  MeV, i.e., as if RMF effects were absent. This is to be expected, since these effects become less significant with decreasing density (cf.  $\Delta U$  profiles in Figs. 1 and 2). In the specific conditions of point F,  $\Delta U$  is negligible with respect to the bare nucleon mass difference (see Table II), therefore (inverse) neutron decays only create (absorb) electron antineutrinos with sub-MeV energies. For the same reason,  $e^+$  captures and absorptions on protons are now relevant over a wide range of the  $\bar{\nu}_e$  spectrum, down to  $\sim 2$  MeV, providing a higher emissivity compared to the other processes and a mean free path that is on average closer to the one associated with  $\bar{\nu}_e N$  scattering reactions with respect to what was observed in Figs. 3 and 4.

For conditions at points A and B, different assumptions on the shape of the neutrino distribution functions do not impact on the emissivities and inverse mean free paths, due to the fact that the reconstructed  $f_\nu$  are very close to the equilibrium ones (see bottom panels of Figs. 3 and 4). Conversely, for point F, we observe qualitative differences depending on the choice of  $f_\nu$ . In fact, neutrinos have already decoupled from matter in the region under consideration, therefore assuming a distribution function at equilibrium is not a good description of the actual neutrino occupation number in the system. Both the emissivity for inelastic NEPS reactions and the inverse mean free path for processes involving  $\nu\bar{\nu}$  pairs are overestimated in the case of equilibrium  $f_\nu$ , as a result of the higher occupation numbers predicted for (anti)neutrinos

in the initial state. The mismatch is more evident in the case of heavy-type neutrinos, for which the decoupling occurs at higher densities with respect to  $\nu_e$  and  $\bar{\nu}_e$  (see Sec. VC). In fact, we notice that the most important process for  $\nu_x$  emission depends on the specific assumption made on  $f_\nu$ . When considering equilibrium conditions, NEPS dominates the overall  $\nu_x$  production, as the corresponding emissivity is overestimated up to  $\sim 2$  orders of magnitude for  $k \lesssim 20$  MeV. On the other hand, when reconstructing  $f_\nu$  from local M1 radiation quantities,  $\nu_x$  up to  $k \sim 10$  MeV are most efficiently produced by other reactions (i.e., NN bremsstrahlung and  $e^+e^-$  annihilations), while  $\nu_x e^\pm$  scattering dominates only at higher energies. Similar differences are observed for the inverse mean free paths associated with the production of  $e^+e^-$  pairs and the inverse NN bremsstrahlung. However, the  $\nu_x$  opacity is dominated in any case by isoenergetic scattering reactions, since inelastic processes become irrelevant once the decoupling from matter has occurred.

## B. Scattering off electrons and positrons

We now focus specifically on the importance of including the contribution of inelastic scattering reactions off electrons and positrons. In Fig. 6 we present the intersection between the energy-dependent neutrino surfaces and the  $xy$  plane for each of the three neutrino species. The optical depths are evaluated using the equilibration

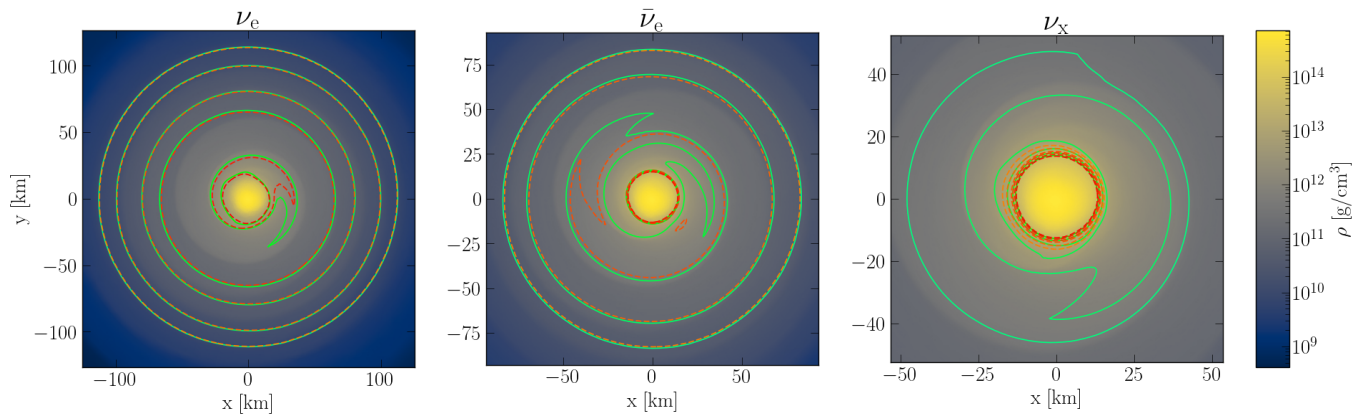


FIG. 6. Energy-dependent, equilibration neutrino surfaces on the  $xy$  plane, with (solid green) and without (dashed red) the contribution of inelastic scattering reactions off electrons and positrons. Color coded is the rest mass density on the plane. Each panel refers to a given neutrino species, i.e.,  $\nu_e$ ,  $\bar{\nu}_e$ , and  $\nu_x$ , from left to right. Different color saturations are used to distinguish the neutrino surfaces of the following energies: 3, 5, 7.5, 10, 17.5, and 25 MeV, moving from inner to outer regions. Note the different spatial resolutions in the panels due to the different typical size of the neutrino surfaces.

inverse mean free path,  $\lambda_{\text{eq}}^{-1}$ , defined in Eq. (42), which is obtained by either summing over all the reactions listed in Sec. II B (solid green) or all the reactions except for NEPS (dashed red). We compute the neutrino surfaces for six energies: 3, 5, 7.5, 10, 17.5, and 25 MeV, where the largest (smallest) neutrino energy corresponds to the outermost (innermost) surface. The surfaces are superimposed to the rest mass density in  $\text{g cm}^{-3}$  on the  $xy$  plane, for reference. In the mean free path calculations, the neutrino distribution functions are reconstructed from the gray M1 radiation quantities.

The left panel of Fig. 6 shows that the effect of NEPS on the thermalization of  $\nu_e$  is marginal, as only the decoupling of neutrinos with 5 MeV is visibly affected when including its contribution. This is a consequence of NEPS having a strong dependence on the matter temperature. Generally, the thermalization of  $\nu_e$  neutrinos occurs mainly through  $\beta$  processes or, for soft neutrinos at high densities, via inverse NN bremsstrahlung. However, when the temperature is large enough, the inverse mean free path for NEPS can be comparable to or larger than the one of the other reactions, as occurs in the hot annulus of matter with  $T \lesssim 40$  MeV (see Fig. 1). This region includes the outer part of the central massive remnant and the innermost part of the disk and is where the surface for  $\nu_e$  with  $k = 5$  MeV is located. In the middle panel, we notice how, for each energy and for both of the sets of reactions considered, the electron antineutrino surfaces have smaller size compared to the electron neutrino ones. This is mostly due to the overabundance of neutrons with respect to protons inside the remnant, which makes absorptions on protons less efficient than the ones on neutrons. In fact, the position of the two outermost  $\bar{\nu}_e$  surfaces is, again, primarily determined by  $\beta$  processes, coherently with the fact that they are pushed outward by only  $\sim 1$  km when considering also the  $\bar{\nu}_e e^\pm$  scattering. On the other hand, moving deeper inside the

system, we find that the inclusion of NEPS reactions significantly expands the antineutrino surfaces with energies of 10 MeV, whose azimuthally averaged radius increases by  $\sim 6$  km, and, particularly, 7.5 MeV, which would be otherwise superimposed to the surfaces of lower energies in the absence of NEPS. This is explainable as, given the conditions where these surfaces are situated (i.e.,  $\sim 10^{12} - 10^{13} \text{ g cm}^{-3}$ ), NEPS is the dominant inelastic process for  $\bar{\nu}_e$  opacity within the energy interval between a few and  $\sim 10$  MeV (see Figs. 13 and 14). The right panel instead clearly shows that for BNS merger conditions, heavy-type neutrinos are the most affected by the inclusion of NEPS reactions. In absence of them, the possibility for  $\nu_x$  to interact via inelastic reactions (typically  $\beta$  processes) is greatly reduced compared to electron-flavored (anti)neutrinos, following from the fact that the  $\mu^\pm$  are not usually included in simulations and  $\tau^\pm$  are not expected to be present in the remnant. In fact, the dashed-red neutrino surfaces of different energies are all concentrated on the edge of the massive central remnant, where the density and temperature drop determines the freeze-out of inverse NN bremsstrahlung and  $\nu_x \bar{\nu}_x$  pair annihilations. On the other hand, when including NEPS, the volume of the region where heavy-type neutrinos equilibrate with matter considerably increases, particularly for the two highest energies considered. Of notable interest is the impact on the surface of 25 MeV neutrinos (close to mean energy typically expected by current models for the emitted  $\nu_x$  spectrum; see, e.g., [10, 43]), whose average radius increases from  $\sim 16$  km to  $\sim 45$  km. The modification of this surface is, likely, directly connected to a variation of the mean energy, since the decoupling from matter occurs at different thermodynamics conditions. In particular, the  $\nu_x$ 's mean energy is expected to decrease since the equilibrium with matter is now preserved out to regions where the fluid is more than 1 order of magnitude less dense and  $\sim 3$  MeV colder.

### C. Impact of weak magnetism, RMF effects, and nucleon decays

The red and purple dot-dashed lines in Figs. 3 and 4 represent the neutrino spectral emissivity and inverse mean free path due to  $\beta$  processes when no microphysics effects are included. The direct comparison with the red and purple solid lines in the same panels highlights the importance of weak magnetism and RMF effects. At the same time, the comparison between red and purple lines addresses the importance of (inverse) nucleon decays and their dependence on the inclusion of microphysics effects.

While  $j_{\beta, \nu_e}$  is insensitive to the inclusion of microphysics effects for  $k \gtrsim \mu_e$  (roughly corresponding to the  $\nu_e$  mean energy in the case of a very degenerate electron gas, i.e.,  $\sim TF_5(\eta_e)/F_4(\eta_e) \sim (6/5)\mu_e$ ), below that threshold it is significantly enhanced (up to 4 orders of magnitude), mostly by RMF effects. Because of detailed balance, also the inverse mean free path is increased by a similar amount below the electron Fermi energy. On the other hand, weak magnetism slightly suppresses  $\lambda_{\beta, \nu_e}^{-1}$  above  $\sim 200$  MeV, independently on the thermodynamic conditions. In the case of electron antineutrinos, the emissivity is marginally increased (up to a factor of a few, note the many orders of magnitude spanned by the vertical axes) by the inclusion of RMF effects (compensating for the attenuation induced by the weak magnetism) for antineutrino energies above the mean production energy by positron captures, i.e.,  $k \gtrsim TF_5(-\eta_e)/F_4(-\eta_e) \sim 5T$ . Below that value, the presence of  $\Delta U > 0$  kinematically suppresses positron captures (see Sec. IV A), but the additional emissivity contribution from neutron decays largely compensates for it, especially for soft antineutrinos. Concerning  $\lambda_{\beta, \bar{\nu}_e}^{-1}$ , we again observe a partial suppression at high antineutrino energies due to weak magnetism and a significant enhancement at low energies induced by the inclusion of inverse neutron decays. We conclude that, overall, weak magnetism, RMF effects, and (inverse) nucleon decays have a significant impact on  $\beta$  processes, possibly affecting the diffusion and the equilibration timescales.

We would like to estimate if these effects could also affect the spectrum of neutrinos streaming at a large distance from the remnant. Using an approach similar to the one presented in Sec. IV B, in Fig. 7 we compare the energy-dependent, equilibrated neutrino surfaces for the decoupling of electron-type (anti)neutrinos obtained by considering two different treatments for the opacities for  $\beta$  processes. The dashed red lines refer to the case in which only bare inverse mean free paths for absorptions on nucleons are employed, as presented in Ref. [70], while solid green ones to the case in which weak magnetism, RMF effects, and inverse nucleon decays are accounted for. The left panel in Fig. 7 shows that only the electron neutrino surfaces at lower energies, i.e., 3 and 5 MeV, are affected when considering an improved description of  $\beta$  processes. The regions enclosed by these two surfaces are enlarged following the enhancement of

$\nu_e n$  absorptions for neutrinos below the  $\nu_e$  mean energy. This effect is entirely ascribable to the inclusion of  $\Delta U$ , which ranges between  $\sim 0.3$  MeV and  $\sim 8$  MeV in correspondence of the decoupling conditions (cf. Fig. 1), since weak magnetism only impacts the opacities of  $\nu_e$  neutrinos with  $k \gtrsim 200$  MeV and inverse proton decays are kinematically suppressed everywhere. Neutrino surfaces of higher energy are not modified as  $\Delta U$  becomes subdominant to the bare nucleon mass difference when moving to outer and less dense regions. The situation in the electron antineutrino case is more varied, as shown in the right panel of Fig. 7, since several of the included effects reveal to be significant, depending on the thermodynamic conditions. Weak magnetism reduces  $\lambda_{\beta, \bar{\nu}_e}^{-1}$  everywhere, but its importance increases with the antineutrino energy, coherently with the fact that it includes the phase-space reduction due to the nucleon recoil as well. Therefore, it affects particularly the outermost surfaces, as high-energy antineutrinos decouple at lower matter densities. Indeed, we observe a shrinkage of antineutrino surfaces with  $k \geq 10$  MeV that is directly connected to the inclusion of weak magnetism, as they are located at densities  $\lesssim 10^{12}$  g cm $^{-3}$ , where  $\Delta U$  is negligible and inverse neutron decays consequently only absorb sub-MeV antineutrinos. Moving to inner regions, RMF effects become more relevant given the progressively higher  $\Delta U$  values, and combine with weak magnetism in decreasing the opacity of  $\bar{\nu}_e p$  absorptions when  $\rho \gtrsim 10^{12}$  g cm $^{-3}$  (cf. Figs. 13 and 14). The marginal reduction in the size of  $\bar{\nu}_e$  surfaces at 7.5 and 5 MeV is in fact a result of the interplay of the two effects. Moving to lower antineutrino energies, decoupling at even higher densities, the impact of weak magnetism becomes negligible while the nucleon interaction potential difference at some point surpasses the energy of the particle experiencing last scattering with matter. Recall that RMF effects change the energy threshold of  $\beta$  processes, such that all electron antineutrinos with  $k \lesssim \Delta m^* + \Delta U$  are absorbed via inverse neutron decays rather than interacting only with protons. As a result, inverse neutron decays push the innermost antineutrino surface ( $k = 3$  MeV) to slightly larger radii, since they occur more frequently than  $\bar{\nu}_e p$  absorptions would in the absence of RMF effects (cf. Fig. 4).

## V. RESULTS: ENERGY INTEGRATED OPACITIES

### A. Reaction comparison

The discussion in Sec. IV focuses on the role of the different reactions in relation to the neutrino energy. However, depending on the local thermodynamic and radiation conditions, some energies could be more relevant than others. Gray emissivities and opacities (see Sec. II C) are informative in this respect, as they account for the distributions of reacting particles. Figure 8 compares the gray absorption and scattering opacities for dif-

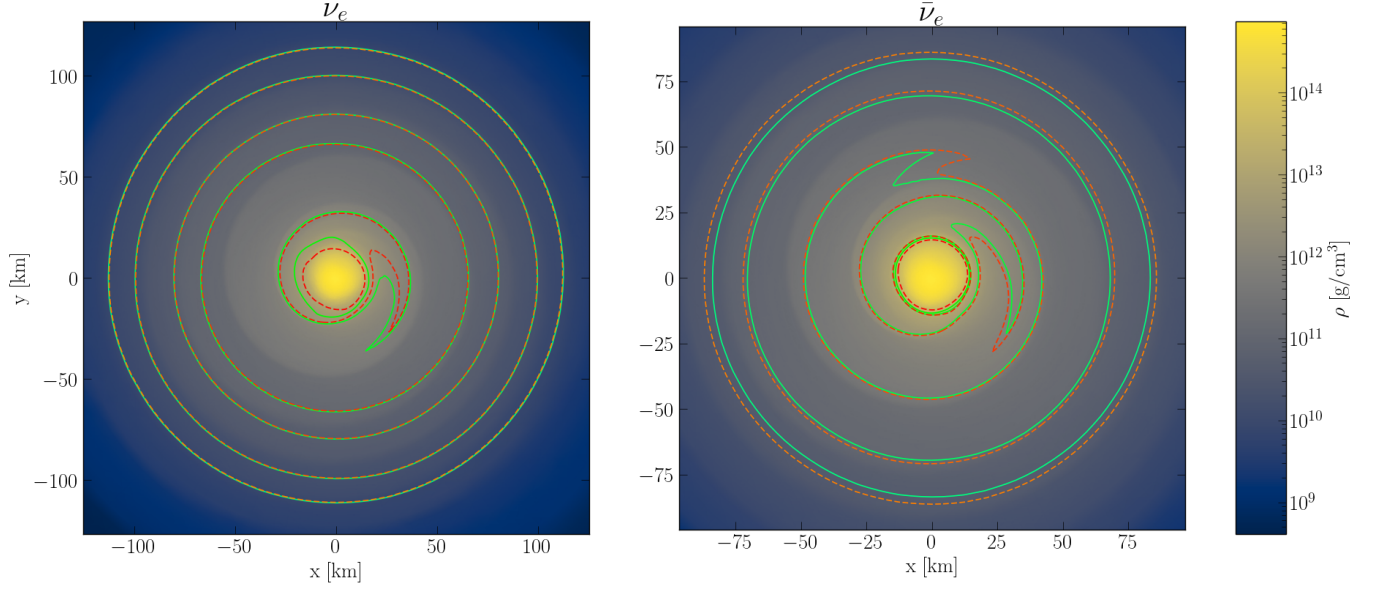


FIG. 7. Energy-dependent, equilibration neutrino surfaces on the  $xy$  plane, obtained with two different treatments for the opacities of  $\beta$  processes. Dashed red lines refer to the case in which only bare inverse mean free paths for absorptions on nucleons are employed, while solid green ones to the case in which weak magnetism, RMF effects and inverse nucleon decays are accounted for. Color coded is the rest mass density on the plane. The left (right) panel refers to electron (anti)neutrinos. Different color saturations are used to distinguish the neutrino surfaces of the following energies: 3, 5, 7.5, 10, 17.5, and 25 MeV, moving from inner to outer regions. Note the different spatial resolutions in the two panels due to the different typical size of the neutrino surfaces.

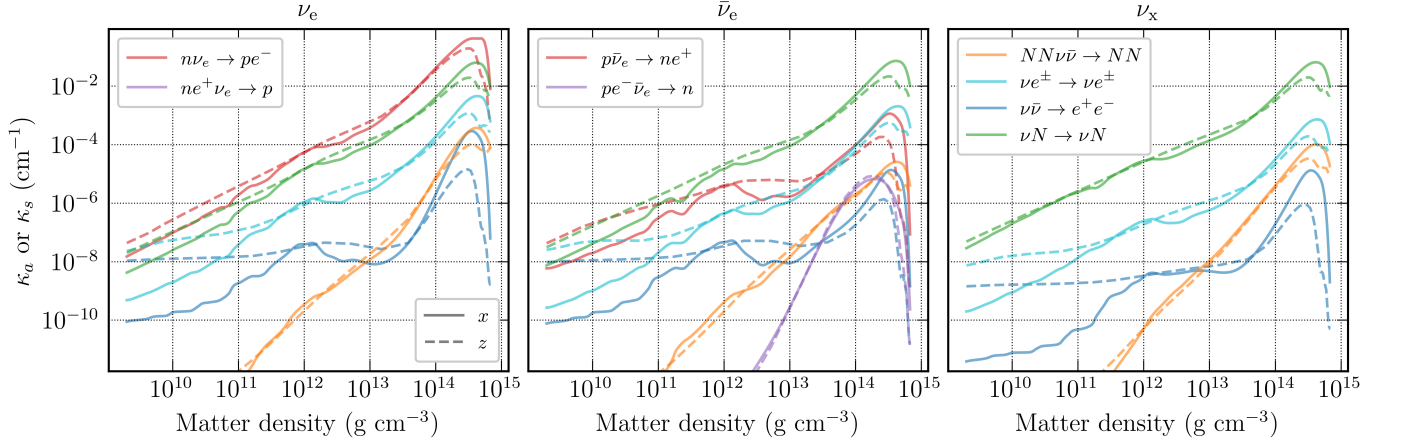


FIG. 8. Gray absorption and scattering opacities as a function of the rest mass density along the positive  $x$  (solid) and  $z$  axis (dashed) of the numerical simulation under study. Different colors refer to the contribution of different reactions, while different panels to different neutrino flavors.

ferent reactions, computed according to Eqs. (22) and (23), for the profiles depicted in Fig. 1 (solid lines) and Fig. 2 (dashed lines), i.e., along the positive  $x$  and  $z$  axis of the simulation under consideration. In the very center of the remnant ( $\rho \approx 7 \times 10^{14} \text{ g cm}^{-3}$ ), the main contribution to the opacity of electron neutrinos (left panel) comes from isoenergetic scattering off nucleons and  $\beta$  processes. In these conditions, the latter are partially suppressed by the Pauli blocking of the dense electron gas. At slightly lower densities ( $\rho \sim \text{a few } 10^{14} \text{ g cm}^{-3}$ ), where

the temperatures are on average larger, i.e.,  $T \lesssim 45 \text{ MeV}$  (20 MeV) along the  $x$  ( $z$ ) axis, cf. Fig. 1 (Fig. 2), the efficiency of  $\nu_e n$  absorptions increases sharply since electrons are less degenerate. As a consequence, when moving away from the center, the absorption opacity of  $\nu_e$  neutrinos surpasses in magnitude the scattering one. The former is primarily contributed by  $\beta$  processes also in the outer part of the profiles. In fact, the integrated opacities for the other inelastic reactions seem to be subdominant everywhere, consistently with the behavior of spec-

tral emissivities and inverse mean free paths discussed in Sec. IV A.

Differently from the electron neutrino case, the opacity for electron antineutrinos (middle panel) is dominated by isoenergetic scattering off nucleons for any condition along the profile, except for its very outer part ( $\rho \lesssim$  a few  $10^{10} \text{ g cm}^{-3}$ ) where its contribution becomes comparable to the one of other inelastic reactions. Neutron degeneracy inhibits  $\bar{\nu}_e p$  absorptions at the highest densities, making scattering off  $e^\pm$  the most efficient channel through which electron antineutrinos exchange energy with matter deep inside the remnant. The  $\bar{\nu}_e$  opacity associated with  $\beta$  processes grows along the  $x$  ( $z$ ) axis in correspondence of the region with higher temperatures, but it does not exceed the one for  $\bar{\nu}_e e^\pm$  scattering until  $\rho \lesssim 10^{14} \text{ g cm}^{-3}$  ( $4 \times 10^{13} \text{ g cm}^{-3}$ ). Pauli blocking of neutrons in the center also impacts the opacity associated with inverse neutron decays, whose shape closely follows the one of  $\Delta U$  as it determines how extended is the energy range over which this process is active (see discussion in Sec. IV A). Nonetheless, even where  $\Delta U$  peaks, inverse neutron decays are not as important as other reactions, since they only absorb (relatively) soft neutrinos which do not weight much on the energy-averaged opacity.

Heavy-type neutrinos (right panel) primarily diffuse within the fluid through isoenergetic scattering off nucleons at any density, as a result of the inability of charged-current processes. Among the inelastic reactions, they are mostly subject to NEPS given the conditions along the profiles. Inverse NN bremsstrahlung partially contributes at high enough densities ( $\rho \gtrsim 10^{14} \text{ g cm}^{-3}$ ), but at larger radii its relevance rapidly fades away due to the strong density dependence of the reaction and to its pair nature. We also notice how the conversion of  $\nu\bar{\nu}$  pairs into  $e^+e^-$  is typically subdominant, for any flavor, down to  $\sim 10^{13} \text{ g cm}^{-3}$ , while it becomes more relevant than the inverse NN bremsstrahlung below that density, since it only depends on the neutrino density and not also on the matter density.

According to Fig. 8, the magnitudes and the reaction hierarchy of the energy-integrated opacities are qualitatively in agreement when comparing their dependence along the  $x$  and  $z$  axes. Nonetheless, we still observe some minor differences that are common to different flavors and reactions. Opacities along the  $x$  axis peak at higher values as a result of the higher peak temperature of matter on the equatorial plane (cf. Figs. 1 and 2). On the other hand, opacities along the  $z$  axis exhibit a shallower decrease in optically-thin conditions, i.e., for  $\rho \lesssim 10^{11} - 10^{12} \text{ g cm}^{-3}$ . This is a combined effect of the dependence of the opacity on the local neutrino density, whose dilution factor depends on the inverse squared distance from the central remnant, and of the sharper density decrease along the  $z$  direction. Therefore, for a given  $\rho$ , neutrinos are more abundant along the polar direction than on the equator, as the given density corresponds to a smaller distance to the center.

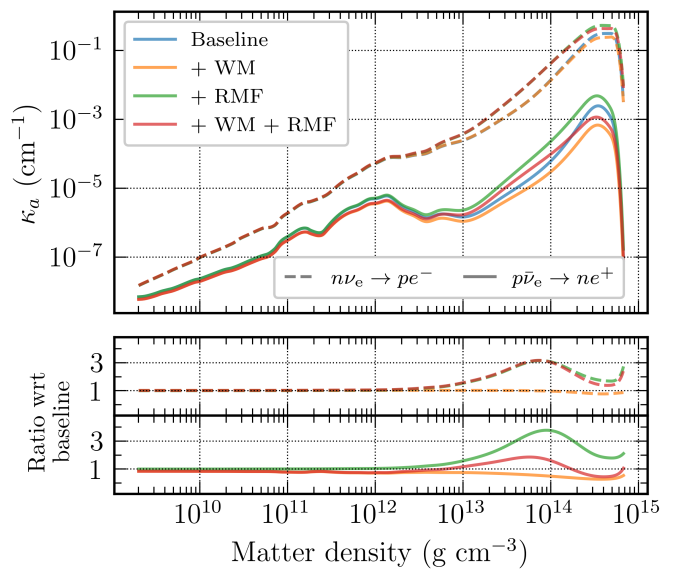


FIG. 9. Top panels: impact of different effects on the gray absorption opacity associated with neutrino absorptions on nucleons as a function of the matter density along the positive  $x$  axis. Middle and bottom panels: ratios with respect to the bare opacity. Dashed (solid) lines refer to  $\nu_e n$  ( $\bar{\nu}_e p$ ) absorptions. The bare absorption opacity is shown in blue, the one accounting only for weak magnetism in orange, the one accounting only for RMF effects in green, while the one including both of them in red.

## B. Impact of weak magnetism and RMF effects

Figure 9 exhibits the impact of weak magnetism and RMF effects on the gray absorption opacity associated with the absorption of electron neutrinos (dashed curves) and antineutrinos (solid curves) on nucleons, as a function of the matter density along the positive  $x$  axis. Inverse nucleon decays are affected by these effects too, but we do not consider them here as their contribution to the total  $\kappa_{a,x}$  is subdominant, or even totally negligible, as shown in Fig. 8. We observe that the opacity of electron neutrinos is mostly affected by the nucleon interaction potential shift,  $\Delta U$ , which increases the efficiency of  $\nu_e n$  absorptions up to a factor of  $\sim 3$  in the inner regions ( $\rho \gtrsim 10^{13} \text{ g cm}^{-3}$ ). On the other hand, the impact of weak magnetism is only marginal and limited to supranuclear densities. In the case of electron antineutrinos, the two effects compete with each other for high enough densities. RMF effects can increase the magnitude of the spectral stimulated  $\bar{\nu}_e$  absorptivity up to a factor of a few at relevant energies (see Sec. IV C), but, at the same time,  $\Delta U$  shifts the kinematic energy threshold of the reaction, increasing the lower limit on the energy of antineutrinos that can be absorbed on protons. Therefore, in the regions where RMF effects are relevant, the enhancement is partially weakened once we weight the spectral integrand by the antineutrino occupation number when computing the energy-integrated opacity. This

is reflected by the fact that the RMF-over-bare opacity ratio does not follow exactly the shape of the  $\Delta U$  distribution along the profile (cf. Fig. 1). It peaks instead at slightly lower densities than  $\Delta U$ , where the influence of  $\bar{\nu}_e p$  absorptions extends over a wider energy range. Conversely, the ratio is lower than one in the case of weak magnetism because it decreases the magnitude of the spectral stimulated  $\bar{\nu}_e$  absorptivity, with a reduction that is more and more significant as antineutrinos are more energetic. Therefore, the impact on the integrated opacity becomes milder when moving to larger radii, because the fraction of high-energy antineutrinos becomes progressively less significant. However, differently from RMF effects, the impact due to weak magnetism survives down to  $\rho \sim 10^{10} - 10^{11} \text{ g cm}^{-3}$ , affecting the typical energy of electron antineutrinos that are emitted from the system (see Sec. IV C).

### C. Estimating the optically thin opacities vs reconstructing the neutrino distribution function

Gray neutrino transports require the knowledge of neutrino distribution functions for the evaluation of energy-integrated emissivities and opacities. However, many approximated schemes that are nowadays employed in simulations do not contain the full information about  $f_\nu$ . One common strategy is to assume equilibrium distributions at the fluid temperature and composition. As this assumption is not well justified in optically thin conditions, the computation of the opacities could be affected by some systematics, especially in the case of  $\nu\bar{\nu}$  processes due to their nonlinear dependencies on the distribution functions. In order to account for that, the gray absorption and scattering opacities are usually corrected in the way presented in Appendix IID.

We discuss hereafter how opacities are affected by the specific assumptions made on the distribution function. In this respect, Fig. 10 compares the total absorption opacity along the positive  $x$  axis in the case of  $f_\nu$  reconstructed from local M1 neutrino quantities or assuming equilibrium conditions (see Sec. IID), eventually corrected by Eq. (39). As expected, from a given density on, the two approaches are no longer in agreement. This corresponds to the point where neutrinos decouple from the matter, which occurs around  $\rho \sim 2 \times 10^{11} \text{ g cm}^{-3}$  for electron neutrinos,  $\rho \sim 4 \times 10^{11} \text{ g cm}^{-3}$  for electron antineutrinos and  $\rho \sim 2 \times 10^{13} \text{ g cm}^{-3}$  for the other neutrino flavors. Nonetheless, in the case of  $\nu_e$  and  $\bar{\nu}_e$ , the correction introduced on the equilibrium opacities is still able to reproduce with a good accuracy the ones reflecting the local radiation properties, even in optically thin conditions. The correction for heavy-flavored neutrinos also starts to be effective once the decoupling happens, but it overestimates the correct opacity by a factor of a few. We can therefore conclude that using a blackbody distribution function, eventually correcting opacities to account for the local temperature in optically

thin regimes, works reasonably well when dealing with electron (anti)neutrinos. In the case of heavy-flavored (anti)neutrinos, more attention should be paid.

## VI. PERFORMANCE OF BNS\_NURATES

BNS\_NURATES is fully integrated with KOKKOS, a C++ library that enables single source performance portable codes [104, 105]. Thanks to this design, the library can run efficiently both on central processing units (CPUs) and GPUs. In the latter case, the computation of spectral or energy-integrated emissivities and opacities at different grid points can be offloaded to multiple GPU cores. We provide here an evaluation of the performance of BNS\_NURATES on CPUs and accelerators, employing the supercomputing cluster PERLMUTTER at NERSC [106]. For CPU runs, the code was compiled with OPENMP and was run on a single node with two AMD EPYC 7763 CPUs, totaling 128 cores. This is compared with performance on a single Nvidia A100 GPU. We ran a test problem in which the integrated (number and energy) emissivities and opacities for all reactions are computed for thermodynamic conditions chosen randomly from a CCSN profile on three dimensional grids with  $16^3$ ,  $32^3$ ,  $64^3$ ,  $128^3$ , and  $192^3$  points. We repeated the test considering two different numbers of quadrature points for the numerical integration routine, namely  $n = 10$  and  $n = 20$  (see Appendix B).

As can be seen in Fig. 11, for a small number of points ( $N_x = 16^3$ ), the performance of BNS\_NURATES on the GPU is worse than on the CPUs. This is likely due to the intrinsic overhead associated with KOKKOS in offloading operations on the GPU cores not being offset by the increased computation speed. For increased computational loads, however, the code is significantly more performing on a single GPU, in this case by a factor of  $\sim 5$ . In the physical scenario of BNS merger simulations that we target, the typical number of points in the computational domain can be very large, so that BNS\_NURATES will operate in this latter regime. We are indeed planning to integrate BNS\_NURATES with the GPU-based hydrocode ATHENAK [107]. Doubling the number of quadrature points on each integration axis causes a performance hit by a factor of  $\sim 3.5 - 3.8$  for  $N_x > 64$ , i.e., consistent with, but somewhat smaller than, the factor of 4 that would be expected given the quadratic scaling of the number of kernel evaluations with  $n$  (see Appendix B).

## VII. DISCUSSION AND CONCLUSIONS

In this work we have presented BNS\_NURATES, a novel open-source software library designed for performance-portable computation of realistic neutrino-matter interaction rates, with particular focus on regimes relevant to BNS mergers. We have then applied BNS\_NURATES to the evaluation of both spectral and energy-integrated emis-

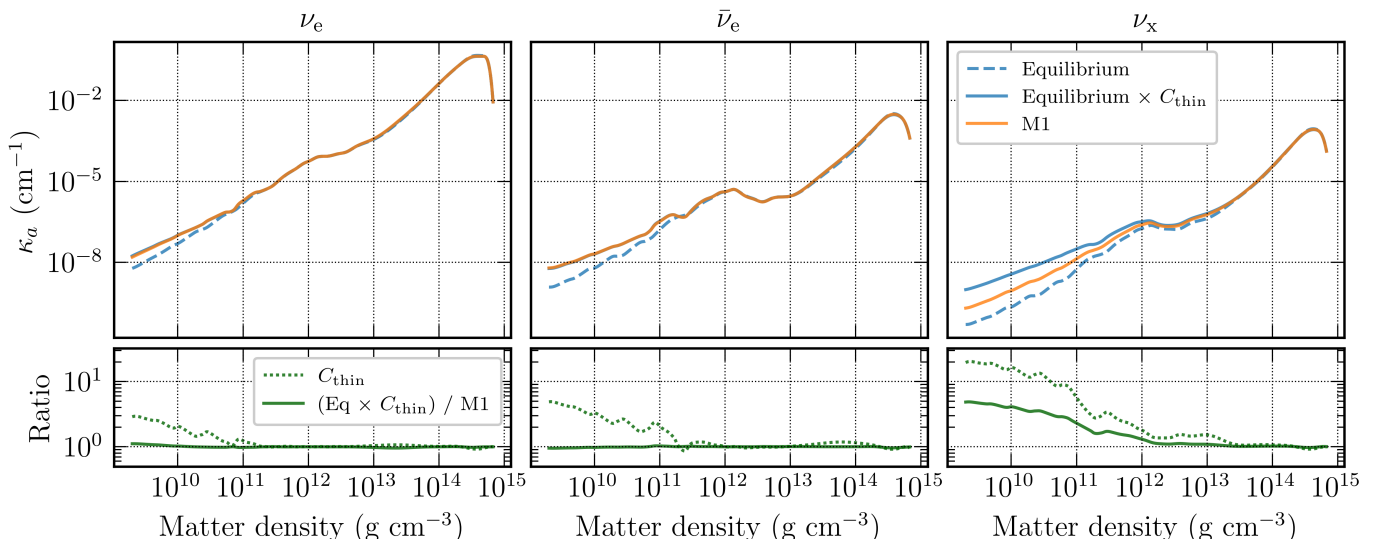


FIG. 10. Top panels: total gray absorption opacities along the positive  $x$  axis obtained reconstructing  $f_\nu$  from M1 radiation quantities (solid orange) or assuming equilibrium  $f_\nu$  (dashed blue), eventually corrected for thin conditions (solid blue) as in Eq. (39). Bottom panels: ratio between the solid curves in the top panels (solid green) and correction factor applied to equilibrium opacities,  $C_{\text{thin}}$  (dotted green), corresponding to the ratio between the blue curves in the top panels. Different panels refer to different neutrino species.

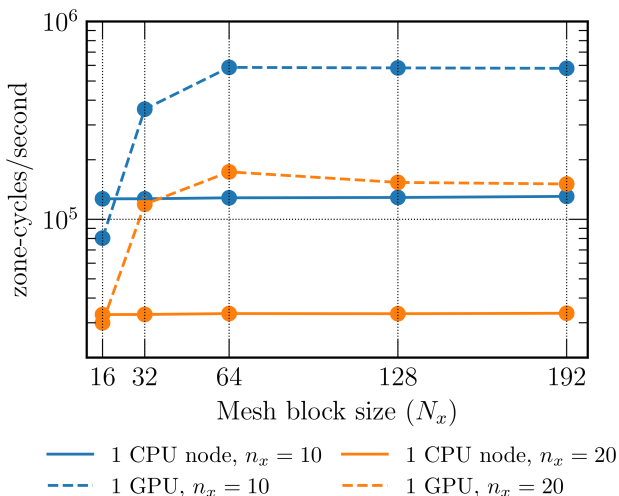


FIG. 11. Central processing unit (CPU) and graphical processing unit (GPU) performance of BNS\_NURATES, measured in zone cycles per second as a function of domain size. For the comparison shown with blue (orange) lines we set  $n = 10$  ( $n = 20$ ) in the quadrature scheme.

sivities and opacities for different conditions extracted from a BNS merger simulation evolved with M1 neutrino transport.

The aim of this study is twofold. On one hand we showcased and tested the capabilities of this new tool. On the other, we provided a general and comprehensive overview of the various reactions undergone by neutrinos of different species for typical BNS merger conditions, employing

a higher degree of accuracy and realism compared to the approaches commonly used in this field. We found that some of the additions and improvements implemented into the library lead to significant differences in the characterization of neutrino interactions in the regimes under consideration. This analysis has highlighted some important aspects, which might stimulate discussion about the current status of neutrino rate modeling in BNS mergers.

We found that inelastic scattering off  $e^\pm$ , an often neglected process in BNS mergers, affects the behavior of heavy-flavored neutrinos in general, as well as the one of electron (anti)neutrinos in very high density regions ( $\rho \sim 7 \times 10^{14} \text{ g cm}^{-3}$ ), where the degeneracy of neutrons and electrons suppresses the importance of  $\beta$  processes. In particular, the inclusion of  $\nu e^\pm$  scattering provides an additional significant contribution to the  $\nu_x$  opacity that pushes the heavy-type neutrino surfaces to outer radii, softening their emission spectrum. This effect is similar to what is observed in the cooling phase of protoneutron stars, see, e.g., [108, 109].

We also showed that weak magnetism and RMF effects can significantly alter  $\nu_e$  and  $\bar{\nu}_e$  bare emissivities and opacities. RMF effects play a relevant role for the dynamics of both species in the regions where the nucleon interaction potential difference,  $\Delta U$ , is non-negligible, i.e.,  $\rho \gtrsim 10^{13} \text{ g cm}^{-3}$ . Weak magnetism is instead more impactful for electron antineutrinos, since, differently from the  $\nu_e$  case, it is important also in outer, less dense regions, affecting the typical conditions at which  $\bar{\nu}_e$  decouple, see, e.g., [71]. We also include the contribution of (inverse) neutron decays, which we found to be particularly relevant for soft  $\bar{\nu}_e$ . Their importance is coupled with the one of RMF effects, as the upper limit on the

energy of antineutrinos they can emit (absorb) is established by the value of  $\Delta U$ , in agreement with previous findings, see, e.g., [65].

BNS\_NURATES attempts to go beyond the assumption of LTE conditions for neutrinos as it exploits gray radiation moments to reconstruct the distribution functions. We tested how the two approaches compare with each other and impact on the interactions. As is to be expected, they differ significantly once the decoupling from matter occurs, but in the case of electron (anti)neutrinos, gray opacities in optically thin conditions can be still correctly estimated even assuming equilibrium, thanks to the application of a correction factor that accounts for the local temperature of the radiation. On the other hand, the opacities of heavy-flavored (anti)neutrinos are still biased even after the introduction of this correction, meaning that a more realistic estimate of the neutrino distribution such as the one we implement is required to avoid the introduction of systematic errors in the opacities.

Despite being informative about the importance of the different neutrino processes in BNS mergers, the present study is still subject to some caveats and limitations. For example, the implemented inelastic reactions do not have any angular dependence, to avoid to perform additional numerical integrations when computing gray emissivities and opacities. In fact, we truncate the Legendre expansion of the reaction kernels at the monopole term (dipole term for the isoenergetic scattering off nucleons). This choice is motivated by the necessity of evaluating neutrino interactions quickly enough to allow *in situ* coupling of BNS\_NURATES to hydrodynamic simulation codes. The library realism could be further increased by considering more terms of the Legendre expansion and by extending the reconstruction of the distribution functions to the angular part, exploiting the additional information about the neutrino flux density.

Furthermore, individual reactions could benefit from an additionally improved treatment. As an example, it is important to assess if the description of the NN bremsstrahlung is reliable enough, as we found that it is the most relevant reaction at very high densities ( $\rho \sim 7 \times 10^{14} \text{ g cm}^{-3}$ ) for soft neutrinos of all flavors. Notice that this is valid despite modeling this process following Ref. [74], which predicts considerably smaller emissivities and opacities at high densities with respect to the more widely adopted, yet less detailed, prescription of Ref. [77] (see also [110] for a comparison in the context of CCSNe). Nonetheless, both approaches rely on a one-pion exchange approximation, which is not appropriate at high densities ( $\rho \gtrsim 10^{14} \text{ g cm}^{-3}$ ). Modified Urca rates, at present absent from our implementation, may also be relevant to accurately describe the precise neutrino dynamics in the central regions of the merger remnant (see, e.g., [12, 14]). An accurate and complete implementation of charged-current reactions is essential to study the dynamical equilibration of the proton fraction via weak interactions and the possible appearance of bulk viscos-

ity, given its potential to alter the postmerger dynamics and its observables; see, e.g., [14, 48, 111–113]. We leave such improvements to future work, but we wish to stress that our publicly available library is going to be actively and continuously maintained and improved. In fact, work on tackling some of the issues mentioned has already started.

Finally, the postprocessing approach we have adopted in this work is of course not fully consistent and cannot capture the dynamical impact of the detailed interactions on the BNS merger system. To do so, BNS\_NURATES should be directly coupled to the neutrino transport scheme employed in a dynamical simulation, evolving the system consistently starting from premerger conditions. Work on achieving this goal is also under way.

## ACKNOWLEDGMENTS

F.M.G. and partially also A.P. are supported by the European Union under NextGenerationEU, PRIN 2022 Project No. 2022KX2Z3B. M.B. and D.R. are supported by the U.S. Department of Energy, Office of Science, Division of Nuclear Physics under Awards No. DE-SC0021177 and No. DE-SC0024388. D.R. also acknowledges support from the Sloan Foundation and from the National Science Foundation under Grants No. PHY-2020275, No. AST-2108467, No. PHY-2116686, and No. PHY-2407681. We acknowledge the EuroHPC Joint Undertaking for awarding this project access to the EuroHPC supercomputer LUMI, hosted by CSC (Finland) and the LUMI consortium through a EuroHPC Extreme Scale Access call (EHPC-EXT-2022E01-046). This research used resources of the National Energy Research Scientific Computing Center, which is supported by the Office of Science of the U.S. Department of Energy under Contract No. DE-AC02-05CH11231.

## DATA AVAILABILITY

Part of the data presented in this manuscript are publicly available [69]. The remaining data supporting the findings of this study will be made available upon reasonable request to the corresponding author.

## Appendix A: REACTION IMPLEMENTATIONS

We report in the following the explicit expressions of the spectral emissivity (for  $\beta$  processes) and kernels (for other reactions), as implemented in BNS\_NURATES. Inverse mean free path and kernels for inverse reactions are consistently computed exploiting the relations reported in Sec. II B. Throughout this section  $G_F \simeq 8.96 \times 10^{44} \text{ MeV cm}^3$  is the Fermi constant,  $\hbar$  is the reduced Planck constant,  $c$  is the speed of light,  $m_e$  is the

electron mass,  $f_{e^\pm}$  is the Fermi-Dirac distribution function for  $e^\pm$ ,  $Q \equiv \Delta m = m_n - m_p \simeq 1.29 \text{ MeV}$  is the bare nucleon mass difference,  $\theta_w \simeq 28.2^\circ$  is the Weinberg angle, and  $g_V = 1$  and  $g_A = 1.23$  are the nucleon form

factors in the zero momentum transfer limit.

*a.  $\beta$  processes.* Following Ref. [70], the spectral emissivity for electron (positron) captures reads as follows:

$$j_{\beta, \nu_e}(k) = \frac{G_F^2 c}{\pi (\hbar c)^4} \eta_{\text{pn}} (g_V^2 + 3g_A^2) (k+Q)^2 \sqrt{1 - \frac{m_e^2}{(k+Q)^2}} f_{e^-}(k+Q) \theta(k+Q - m_e) W(k), \quad (\text{A1})$$

$$j_{\beta, \bar{\nu}_e}(k) = \frac{G_F^2 c}{\pi (\hbar c)^4} \eta_{\text{np}} (g_V^2 + 3g_A^2) (k-Q)^2 \sqrt{1 - \frac{m_e^2}{(k-Q)^2}} f_{e^+}(k-Q) \theta(k-Q - m_e) \bar{W}(k), \quad (\text{A2})$$

where  $\theta$  is the Heaviside step function, which accounts for the reaction kinematics. As we do not account for  $\mu^\pm$  or  $\tau^\pm$  leptons in the system,  $j_{\nu_x}(k)$  and  $j_{\bar{\nu}_x}(k)$  are identically equal to zero  $\forall k$ . The functions  $W(k)$  and  $\bar{W}(k)$  are the energy-dependent corrections due to the sum of phase-space, recoil, and weak magnetism effects and are included following Ref. [71]. The quantities  $\eta_{\text{pn}}$  and  $\eta_{\text{np}}$  account for the nucleon final state blocking:

$$\eta_{\text{pn}} = \frac{n_n - n_p}{\exp\{(\mu_p - \mu_n - Q)/T\} - 1}, \quad (\text{A3})$$

where  $n_p$  ( $n_n$ ) is the proton (neutron) number density and  $\mu_p$  ( $\mu_n$ ) is the proton (neutron) relativistic chemical potential.  $\eta_{\text{np}}$  can be obtained via the replacement  $n \leftrightarrow p$  in Eq. (A3). We also account for in-medium effects associated to nucleon interactions following Refs. [65, 72]. Such effects can be implemented by replacing  $Q$  in Eqs. (A1)-(A3) with the nucleon energy difference within the RMF framework, i.e.,  $Q^* \equiv \Delta m^* + \Delta U$ . Neutrino spectral emissivities resulting from nucleon decays are related to the ones of lepton captures through the crossing symmetry of the captured lepton [65]. In fact, one can recover  $j_{\nu_e}$  and  $j_{\bar{\nu}_e}$  for nucleon decays through the substitutions  $k \rightarrow -k$ ,  $Q^{(*)} \rightarrow -Q^{(*)}$ , and  $f_{e^\pm} \rightarrow 1 - f_{e^\mp}$  in Eqs. (A1) and (A2), respectively.

*b. Pair processes.* For electron-positron annihilations (EPA), the zeroth-order term of the Legendre expansion of the production kernels is modeled as (see [73])

$$R_{\text{EPA},x}^{\text{pro},0}(k, k') = \frac{1}{2\pi} \frac{G_F^2}{\hbar (\hbar c)^3} \frac{T^2}{1 - e^{(y+z)}} \times \quad (\text{A4})$$

$$[\alpha_{1,x} \Psi_0(y, z) + \alpha_{2,x} \Psi_0(z, y)],$$

where  $y \equiv k/T$  and  $z \equiv k'/T$  are the dimensionless energies of the (anti)neutrino with flavor  $x$  and of its corresponding antiparticle, respectively. The coefficients  $\alpha_{1,2}$  are defined as  $\alpha_{1,\nu_e} = 1 + 2 \sin^2 \theta_w$ ,  $\alpha_{1,\nu_x} = -1 + 2 \sin^2 \theta_w$ , and  $\alpha_{2,\nu_e} = \alpha_{2,\nu_x} = 2 \sin^2 \theta_w$ . For antineutrinos, the coefficients are obtained by exchanging  $\alpha_{1,x} \leftrightarrow \alpha_{2,x}$  of the corresponding neutrino. The  $\Psi_0$  function, whose explicit form is reported by Eq. (11) in Ref. [73], is given by a

linear combination of incomplete Fermi-Dirac integrals. We exploit recursive formulas to express them in terms of the complete ones, which we evaluate as described in Ref. [82].

In the case of NN bremsstrahlung channels, the annihilation kernels do not depend on the neutrino species and the monopole term of their Legendre expansion reads ( $C_A = -1.26/2$ )

$$R_{\text{Brem}}^{\text{ann},0}(k, k') = 3 C_A^2 \frac{G_F^2}{\hbar} n_N S_\sigma(n_N; k + k'). \quad (\text{A5})$$

For the  $S_\sigma$  function we adopt the fitting formula provided by Ref. [74], which is based on a one-pion exchange description of the nucleon-nucleon interaction. The quantity  $n_N$  appearing in Eq. (A5) is the nucleon number density for the corresponding bremsstrahlung channel ( $n_n$ ,  $n_p$ ,  $\sqrt{n_n n_p}$  for neutron-neutron, proton-proton, and neutron-proton, respectively). The total kernel is obtained by summing Eq. (A5) over the three channels. We also account for the impact of medium modifications on the process by applying the density-dependent correction factor defined in Ref. [75], which significantly decreases the magnitude of the bare kernel at high densities ( $\gtrsim 70\%$  reduction for  $\rho \gtrsim 10^{14} \text{ g cm}^{-3}$ ).

*c. Scattering processes.* The first two Legendre coefficients of the isoenergetic scattering kernel expansion are defined in Ref. [70] as the following, depending on the target particle  $N \in \{\text{n, p}\}$ :

$$\begin{aligned} \left[ \begin{array}{l} R_{\text{iso}}^0(k, k') \\ R_{\text{iso}}^1(k, k') \end{array} \right] &= 2\pi \frac{G_F^2}{\hbar} \eta_{\text{NN}} \delta(k - k') \times \quad (\text{A6}) \\ &\left\{ \begin{array}{l} [(h_V^N)^2 + 3(h_A^N)^2] W_0^N(k) \\ [(h_V^N)^2 - (h_A^N)^2] W_1^N(k) \end{array} \right\}. \end{aligned}$$

The values of the coupling constants  $h_V^N$  and  $h_A^N$  are reported in Ref. [70] and do not depend on the neutrino species, so the kernel expressions are the same for each  $x$ . The quantity  $\eta_{\text{NN}}$  results from the integration over the nucleon phase-space variables and is computed considering a linear interpolation between the results for the non-degenerate and degenerate limits for nucleons. The

functions  $W_0^N(k)$  and  $W_1^N(k)$  are included to account for phase-space, recoil, and weak magnetism effects associated with neutral-current reactions for the zeroth and first coefficient, respectively. Such functions have been calculated by expanding Eq. (12) in Ref. [71] to first or-

der in  $\omega$ , assuming  $k = k'$ .

In the case of inelastic neutrino-electron (NES) and neutrino-positron (NPS) scattering, the isotropic term in the kernel expansion is computed following the approach in Refs. [70, 76], but performing the integration over the electron energy analytically:

$$R_{(\text{NES/NPS}),x}^{\text{out},0}(k, k') = -\frac{1}{3\pi} \left[ \frac{G_F}{(\hbar c)^3} \right]^2 (\hbar c)^2 T^2 \times \{ [1 - \exp(z - y)] y^2 z^2 \}^{-1} \times \left\{ \frac{\alpha_{1,x}^2 + \alpha_{2,x}^2}{5} [\text{sign}(y - z) A_5^i + D_5^i] + \alpha_{1,x}^2 (y + z) [D_4^i + 2(y + z) D_3^i + 6yz D_2^i] + 6\alpha_{1,x}^2 y^2 z^2 D_1^i - \text{sign}(y - z) [(\alpha_{1,x}^2 M_{y,z} - \alpha_{2,x}^2 m_{y,z}) A_4^i + 2(\alpha_{1,x}^2 M_{y,z}^2 + \alpha_{2,x}^2 m_{y,z}^2) A_3^i] \right\}. \quad (\text{A7})$$

Here,  $M_{y,z} \equiv \max(y, z)$  and  $m_{y,z} \equiv \min(y, z)$  indicate the maximum and minimum, respectively, between  $y = k/T$  and  $z = k'/T$ . We also introduce the functions  $D_n^i = D_n^i(y, z) \equiv F_n(\eta_i - z) - F_n(\eta_i - y)$  and  $A_n^i = A_n^i(y, z) \equiv F_n(\eta_i - |y - z|) - F_n(\eta_i)$  to express subtraction between complete Fermi-Dirac integrals of order  $n$ , where  $\eta_i$  is the degeneracy parameter of  $i = e^-$  ( $i = e^+$ ) in the case of NES (NPS). The total NEPS *out* kernel is obtained by summing  $R_{\text{NES},x}^{\text{out},0}$  and  $R_{\text{NPS},x}^{\text{out},0}$ .

## Appendix B: GAUSSIAN QUADRATURE SCHEME

As discussed in Sec. II C, the evaluation of gray M1 emissivities and opacities requires one- and two-dimensional integrations from zero to infinite neutrino energies. In order to perform the integration, we split the domain into two intervals, one ranging from 0 to  $t_{l,x}$  and the other from  $t_{l,x}$  to  $+\infty$ , with the splitting energy,  $t_{l,x}$ , chosen depending on the reaction  $l$  and the neutrino species  $x$ . We map each interval onto the  $[0, 1]$  segment by a change of variable. The contribution to the total integral of each segment is evaluated via a Gauss-Legendre quadrature scheme with  $n$  points. Let  $\{x_j\}$  and  $\{w_j\}$  with  $j = 1, 2, \dots, n$  be the (dimensionless) quadrature nodes and weights in the  $[0, 1]$  interval, respectively. The integrands are then evaluated at the energies  $k_j = t_{l,x} x_j$  ( $k_j = t_{l,x}/x_j$ ) for the first (second) segment. Therefore, the quadrature of a generic energy-dependent integrand  $G_{l,x}(k)$  reads

$$\int dk G(k) = t \sum_{j=1}^n w_j \left[ G(t x_j) + \frac{G(t/x_j)}{x_j^2} \right], \quad (\text{B1})$$

where we dropped the  $\{l, x\}$  dependence in the interest of readability. In this way, the total number of evaluations of  $G$  in Eq. (B1) is equal to  $2n$ , with  $n$  set by the user at run-time. The results presented in the manuscript

have been obtained by setting  $n = 50$ , unless otherwise specified.

The contribution by  $\beta$  processes to the total emissivity and absorption opacity of  $\nu_e$  ( $\bar{\nu}_e$ ) is evaluated by splitting 1D integrals at the mean energy of (anti)neutrinos emitted via electron (positron) captures [4]:

$$t_{\nu_e} = T \frac{F_5(\eta_e)}{F_4(\eta_e)}, \quad t_{\bar{\nu}_e} = T \frac{F_5(-\eta_e)}{F_4(-\eta_e)}. \quad (\text{B2})$$

Instead, for the gray scattering opacity we split the domain at the local neutrino mean energy, given by the ratio between the zeroth neutrino moments, i.e.,  $t_x = J_x/n_x$ .

Equation (B1) can be easily generalized to treat two-dimensional integration for reactions involving  $\nu\bar{\nu}$  pairs. We employ the same number of integration points on both axes and split both integration domains at the same energy, so that double integrals can be evaluated as

$$\int dk \int dk' \hat{G}(k, k') = t^2 \sum_{j=1}^n \sum_{k=1}^n w_j w_k \times \left[ \hat{G}(t x_j, t x_k) + \frac{\hat{G}(t x_j, t/x_k)}{x_k^2} + \frac{\hat{G}(t/x_j, t x_k)}{x_j^2} + \frac{\hat{G}(t/x_j, t/x_k)}{x_j^2 x_k^2} \right]. \quad (\text{B3})$$

In the case of  $e^+e^-$  annihilations and NN bremsstrahlung, we set  $t$  to half of the average energy of a neutrino-antineutrino couple emitted by NN bremsstrahlung, namely,  $t = 2.182T$  [77]. We use this value also when evaluating the contribution of such reactions to spectral emissivities and inverse mean free paths via 1D integrals (see Sec. II A).

Using the same quadrature prescription for different reactions allows us to sum together the integrands associated to different processes beforehand, avoiding to perform a specific integration for each of them. In this respect, we checked that the contribution of (inverse)

$e^+e^-$  annihilations to the gray emissivities and opacities converges quickly enough with respect to  $n$  even if  $t$  is not specifically tailored to the process. Notice that the number of evaluations of  $\hat{G}$  in Eq. (B3) is equal to  $4n^2$ . However, since the quadrature nodes and weights are the same along the two axes, we can exploit symmetry relations between kernels with  $(k, k')$  and  $(k', k)$  dependence. This reduces by half the number of kernel evaluations necessary, leading to a sizable speed up of the execution.

In the case of NEPS integration, setting  $t$  to the above-mentioned value does not allow to achieve a quick convergence with respect to  $n$ , since the distribution of the quadrature nodes across the domains does not sample efficiently the integrands. In fact, the position where the integrands for NEPS peak depends on the energies of the neutrinos themselves. Therefore, for the evaluation of spectral emissivities and inverse mean free paths for NEPS we set  $t = k$ , corresponding to the position where the value of the integrands is the largest. For the computation of the gray quantities instead, we follow a different paradigm than Eq. (B3). We first apply a rotation of  $45^\circ$  on the integration variables, i.e.,  $u = k+k'$  and  $v = k-k'$ , so that the double integrals can be rewritten as

$$\int dk \int dk' \hat{G}(k, k') = \frac{1}{2} \int_{-\infty}^{+\infty} du \int_{-u}^{+u} dv \hat{G}\left(\frac{u+v}{2}, \frac{u-v}{2}\right). \quad (\text{B4})$$

We then split the innermost integral at  $v = 0$ , rescaling the integration variable into the  $[0, 1]$  interval for both segments and using  $n'$  quadrature points along each of the two. In this way, the sampling of the  $\hat{G}$  function is more efficient, since we are splitting the quadrature nodes evenly across the position of the peak of the integrands, i.e.,  $v = k-k' = 0$ . Please note that  $n'$  can be in principle different than  $n$ , allowing us to use a different number of integration points depending on the reaction. However, in the context of this manuscript we always set  $n' = n$ . We finally exploit Eq. (B1) using  $t' \sim 8T$  and  $n'$  points to deal with the outermost integration over the  $[0, +\infty)$  interval, where  $t'$  was fine-tuned to achieve the quickest convergence. In the end, the formula implemented for evaluating the NEPS contribution to gray emissivities and opacities reads

$$\int dk \int dk' \hat{G}(k, k') = \frac{(t')^2}{2} \sum_{j=1}^{n'} \sum_{k=1}^{n'} w_j w_k \times \left[ x_j \hat{G}(a_{jk}, b_{jk}) + x_j \hat{G}(b_{jk}, a_{jk}) + \frac{\hat{G}(a_{jk}/x_k^2, b_{jk}/x_k^2)}{x_j^3} + \frac{\hat{G}(b_{jk}/x_k^2, a_{jk}/x_k^2)}{x_j^3} \right], \quad (\text{B5})$$

where we defined  $a_{jk} \equiv t'x_j(1-x_k)/2$  and  $b_{jk} \equiv t'x_j(1+x_k)/2$  to lighten the notation.

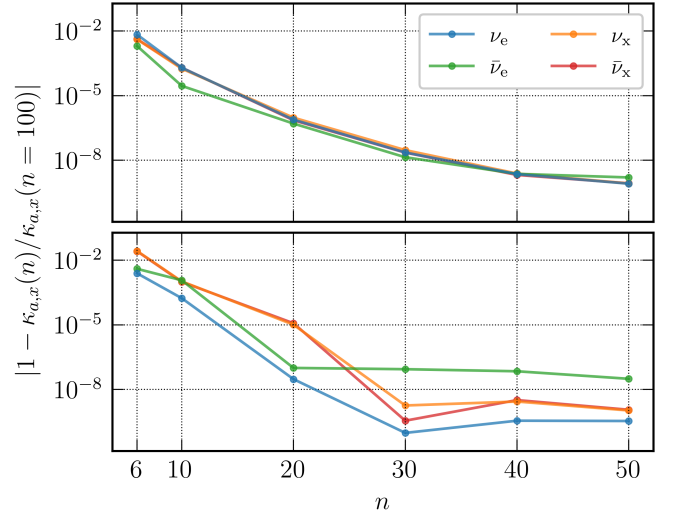


FIG. 12. Top (bottom) panel: convergence level of the total  $\kappa_{a,x}$  with respect to the number of quadrature points for the thermodynamic conditions at point A (F) in Table II, using  $n = 100$  as a reference. Different colors refer to the different neutrino flavors.

Figure 12 shows the convergence in the calculation of the total gray absorption opacity with respect to  $n$ , for the thermodynamic conditions at points A and F in Table II and reconstructing the distribution function through M1 quantities. The relative error in the evaluation of  $\kappa_a$  at point A is below  $10^{-2}$  for all neutrino species already when considering  $n = 6$ , which we identify as a good trade-off in terms of accuracy and performances for the coupling in simulations of BNS\_NURATES to a gray M1 scheme (see Sec. VI). The largest discrepancy with respect to the  $n = 100$  calculation is observed for heavy-type (anti)neutrinos at point F, which is around  $\sim 2\%$  for  $n = 6$ . This is because NEPS is the dominant reaction channel in such conditions and, differently than for the other flavors, the  $\nu_x$  mean energy does not match the energy at which the integral is split ( $\langle E_{\nu_x} \rangle \sim 2t'$ , see Table II), affecting the resolution in the integrand sampling. However, this order of convergence is still reasonable considering the level of accuracy achieved in neutrino transport with M1 schemes. Moreover, the magnitude of the gray opacity at point F is much lower given the smaller density, and so is the absolute error. The level of convergence observed for the other gray quantities, i.e.,  $\tilde{\eta}_x$ ,  $\eta_x$ , and  $\tilde{\kappa}_{a,x}$ , is qualitatively similar to the one shown in Fig. 12.

### Appendix C: OPTICAL DEPTH AND NEUTRINO SURFACE COMPUTATION

In order to compute the optical depths necessary to locate neutrino surfaces for the neutrino species  $x$ , we rely on a variant of the classical Dijkstra's algorithm [114] applied to the three-dimensional data extracted from the

BNS simulation under consideration. This iterative algorithm stores at each iteration an estimate of the optical depth,  $\tau_{\text{est},x}$ , for each cell in the computational domain. This information is augmented by a priority queue which stores the spatial coordinates and the current value of  $\tau_{\text{est},x}$  for a variable number of cells. The queue is sorted in order of ascending optical depth. Initially, every cell is assigned infinite  $\tau_{\text{est},x}$ , except for the boundary cells for which  $\tau_{\text{est},x} = 0$ . The priority queue initially contains the coordinates and the estimated optical depths of the boundary cells only. At every iteration, we pop the first element of the queue, whose coordinates we denote as  $\mathbf{x}$ . Based on its location, we compute a new optical depth's estimate,  $\tau'_{\text{est},x}$ , for every first neighbor of the corresponding cell:

$$\tau'_{\text{est},x}(\mathbf{x}_n) = \tau_{\text{est},x}(\mathbf{x}) + \lambda_x^{-1} \sqrt{\gamma_{ij} \Delta \mathbf{x}^i \Delta \mathbf{x}^j}, \quad (\text{C1})$$

where  $\mathbf{x}_n$  is the position of the  $n$ th neighbor cell;  $\gamma$  is the spatial three-metric;  $\Delta \mathbf{x} := \mathbf{x}_n - \mathbf{x}$  is the coordinate distance between the two cells; and all quantities on the right-hand side are evaluated at  $\mathbf{x}$ . Neutrino reactions enter in Eq. (C1) through the quantity  $\lambda_x^{-1}$ , defined in

Sec. III C. We then compare  $\tau'_{\text{est},x}(\mathbf{x}_n)$  with the previous estimate at the same cell. If  $\tau'_{\text{est},x}(\mathbf{x}_n) < \tau_{\text{est},x}(\mathbf{x}_n)$ , we substitute the latter with the former and we add an element to the priority queue, storing the coordinates  $\mathbf{x}_n$  and the corresponding new optical depth's estimate. These steps are repeated until the queue contains no elements. The algorithm is guaranteed to terminate because the optical depth is always non-negative, therefore it always exhibits a minimum. As such, this procedure allows for the calculation of the optical depth for each cell in the entire computational domain.

#### Appendix D: ENERGY-DEPENDENT EMISSIVITIES AND INVERSE MEAN FREE PATHS FOR ADDITIONAL CONDITIONS

We include in the following the plots exhibiting the spectral emissivities and inverse mean free paths, as well as the neutrino distribution functions, for thermodynamic conditions extracted at the points C, D, and E of Table II (Figs. 13- 15, respectively). They complete the discussion in Sec. IV A by showing the behavior of the various reactions in the transition between optically thick and optically thin regimes.

- 
- [1] F. Foucart, *Liv. Rev. Comput. Astrophys.* **9**, 1 (2023), [arXiv:2209.02538 \[astro-ph.HE\]](#).
  - [2] D. Eichler, M. Livio, T. Piran, and D. N. Schramm, *Nature* **340**, 126 (1989).
  - [3] M. Ruffert, H. Janka, K. Takahashi, and G. Schäfer, *Astron. Astrophys.* **319**, 122 (1997), [arXiv:astro-ph/9606181 \[astro-ph\]](#).
  - [4] S. Rosswog and M. Liebendoerfer, *Mon. Not. Roy. Astron. Soc.* **342**, 673 (2003), [arXiv:astro-ph/0302301](#).
  - [5] L. Dessart, C. Ott, A. Burrows, S. Rosswog, and E. Livne, *Astrophys. J.* **690**, 1681 (2009), [arXiv:0806.4380 \[astro-ph\]](#).
  - [6] A. Perego, S. Rosswog, R. M. Cabezón, O. Korobkin, R. Käppeli, A. Arcones, and M. Liebendörfer, *Mon. Not. Roy. Astron. Soc.* **443**, 3134 (2014), [arXiv:1405.6730 \[astro-ph.HE\]](#).
  - [7] E. Loffredo, A. Perego, D. Logoteta, and M. Branchesi, *Astron. Astrophys.* **672**, A124 (2023), [arXiv:2209.04458 \[astro-ph.HE\]](#).
  - [8] H. Gieg, F. Schianchi, M. Ujevic, and T. Dietrich, [arXiv:2409.04420 \[gr-qc\]](#) (2024).
  - [9] M. A. Pajkos and E. R. Most, *Phys. Rev. D* **111**, 043013 (2025), [arXiv:2409.09147 \[astro-ph.HE\]](#).
  - [10] F. Foucart, R. Haas, M. D. Duez, E. O'Connor, C. D. Ott, L. Roberts, L. E. Kidder, J. Lippuner, H. P. Pfeiffer, and M. A. Scheel, *Phys. Rev. D* **93**, 044019 (2016), [arXiv:1510.06398 \[astro-ph.HE\]](#).
  - [11] F. Zappa, S. Bernuzzi, D. Radice, and A. Perego, *Mon. Not. Roy. Astron. Soc.* **520**, 1481 (2023), [arXiv:2210.11491 \[astro-ph.HE\]](#).
  - [12] E. R. Most, A. Haber, S. P. Harris, Z. Zhang, M. G. Alford, and J. Noronha, *Astrophys. J. Lett.* **967**, L14 (2024), [arXiv:2207.00442 \[astro-ph.HE\]](#).
  - [13] A. Perego, S. Bernuzzi, and D. Radice, *Eur. Phys. J.* **A55**, 124 (2019), [arXiv:1903.07898 \[gr-qc\]](#).
  - [14] P. L. Espino, P. Hammond, D. Radice, S. Bernuzzi, R. Gamba, F. Zappa, L. F. Longo Micchi, and A. Perego, *Phys. Rev. Lett.* **132**, 211001 (2024), [arXiv:2311.00031 \[astro-ph.HE\]](#).
  - [15] S. Wanajo, Y. Sekiguchi, N. Nishimura, K. Kiuchi, K. Kyutoku, and M. Shibata, *Astrophys. J.* **789**, L39 (2014), [arXiv:1402.7317 \[astro-ph.SR\]](#).
  - [16] B. D. Metzger and R. Fernández, *Mon. Not. Roy. Astron. Soc.* **441**, 3444 (2014), [arXiv:1402.4803 \[astro-ph.HE\]](#).
  - [17] D. Martin, A. Perego, A. Arcones, F.-K. Thielemann, O. Korobkin, and S. Rosswog, *Astrophys. J.* **813**, 2 (2015), [arXiv:1506.05048 \[astro-ph.SR\]](#).
  - [18] Y. Sekiguchi, K. Kiuchi, K. Kyutoku, M. Shibata, and K. Taniguchi, *Phys. Rev. D* **93**, 124046 (2016), [arXiv:1603.01918 \[astro-ph.HE\]](#).
  - [19] S. Fujibayashi, Y. Sekiguchi, K. Kiuchi, and M. Shibata, *Astrophys. J.* **846**, 114 (2017), [arXiv:1703.10191 \[astro-ph.HE\]](#).
  - [20] D. Radice, A. Perego, K. Hotokezaka, S. A. Fromm, S. Bernuzzi, and L. F. Roberts, *Astrophys. J.* **869**, 130 (2018), [arXiv:1809.11161 \[astro-ph.HE\]](#).
  - [21] S. Fujibayashi, M. Shibata, S. Wanajo, K. Kiuchi, K. Kyutoku, and Y. Sekiguchi, *Phys. Rev. D* **101**, 083029 (2020), [arXiv:2001.04467 \[astro-ph.HE\]](#).
  - [22] O. Just, S. Goriely, H.-T. Janka, S. Nagataki, and A. Bauswein, *Mon. Not. Roy. Astron. Soc.* **509**, 1377 (2021), [arXiv:2102.08387 \[astro-ph.HE\]](#).

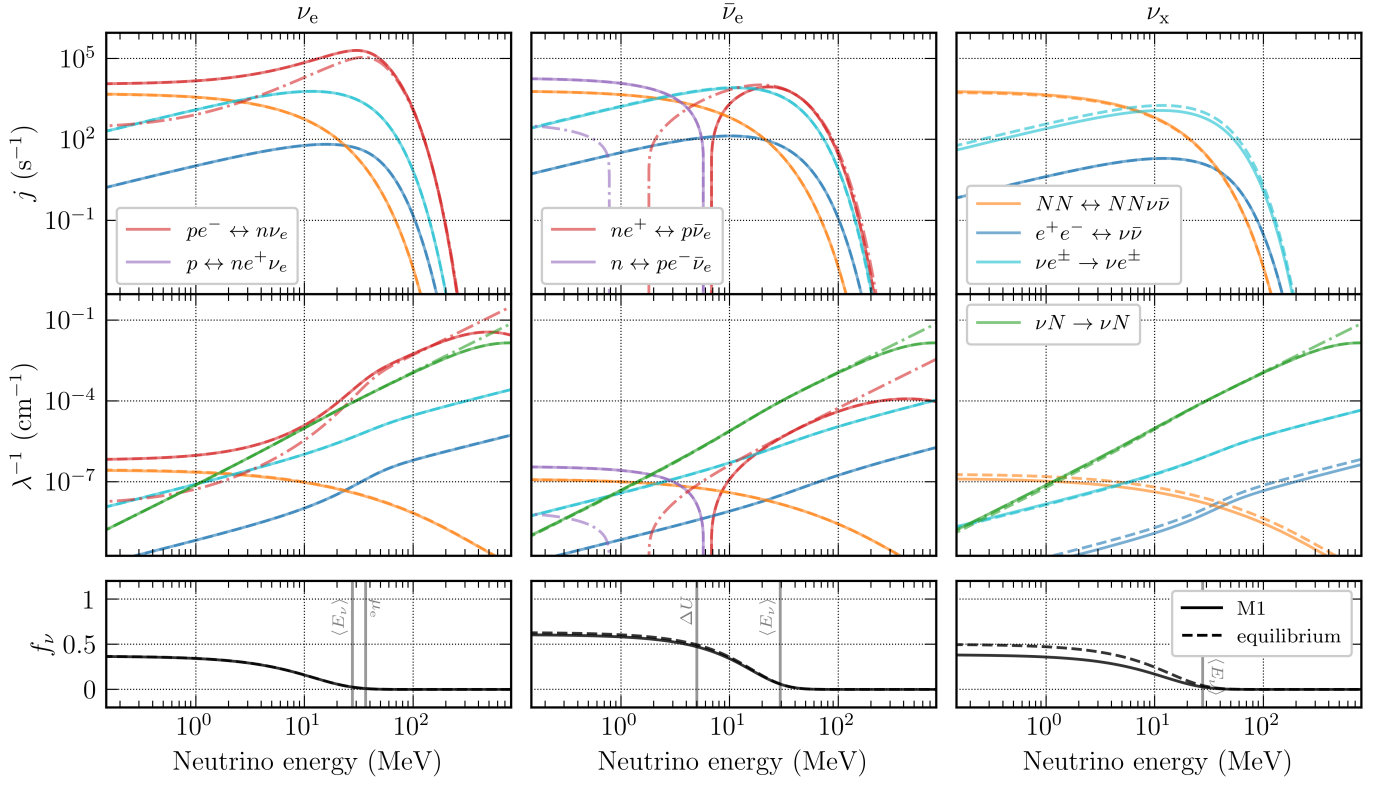


FIG. 13. Same as Fig. 3 but for thermodynamic point C in Table II.

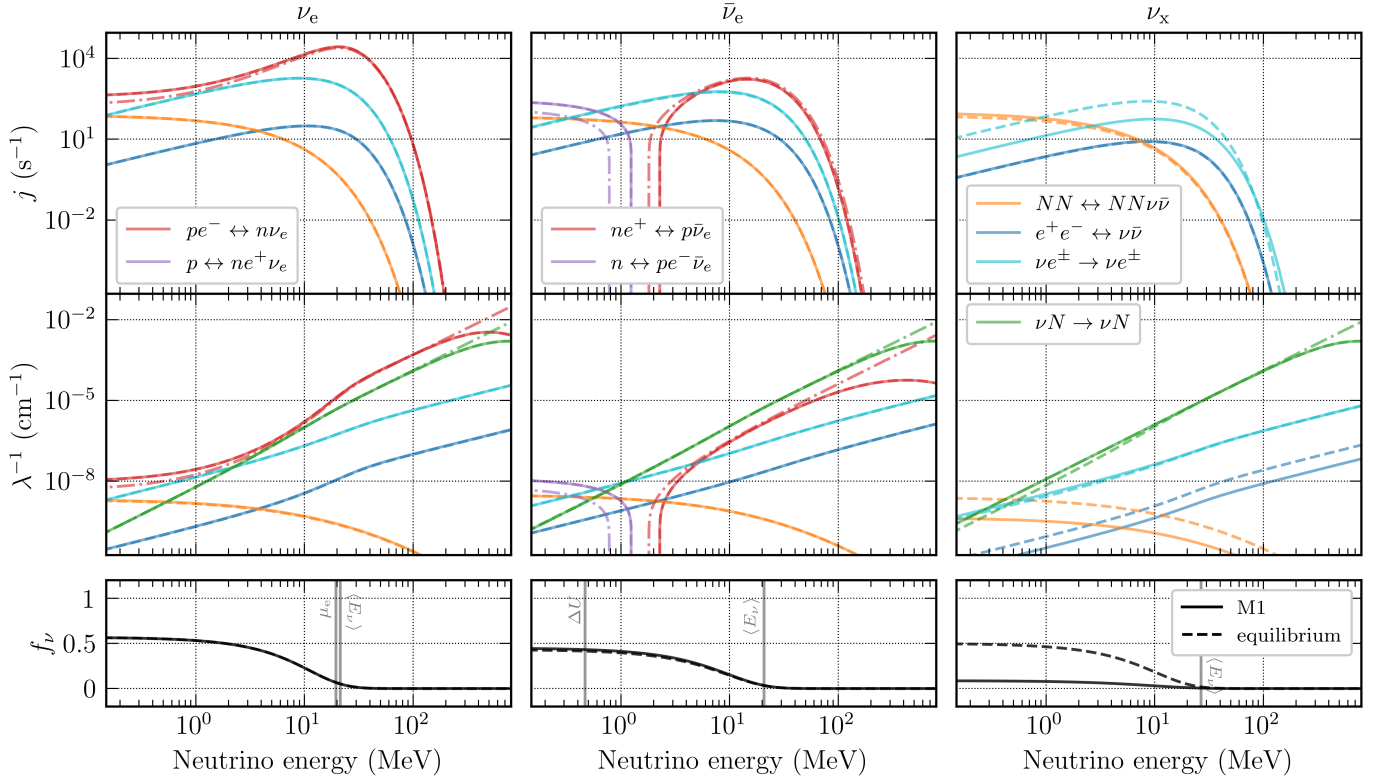


FIG. 14. Same as Fig. 3 but for thermodynamic point D in Table II.

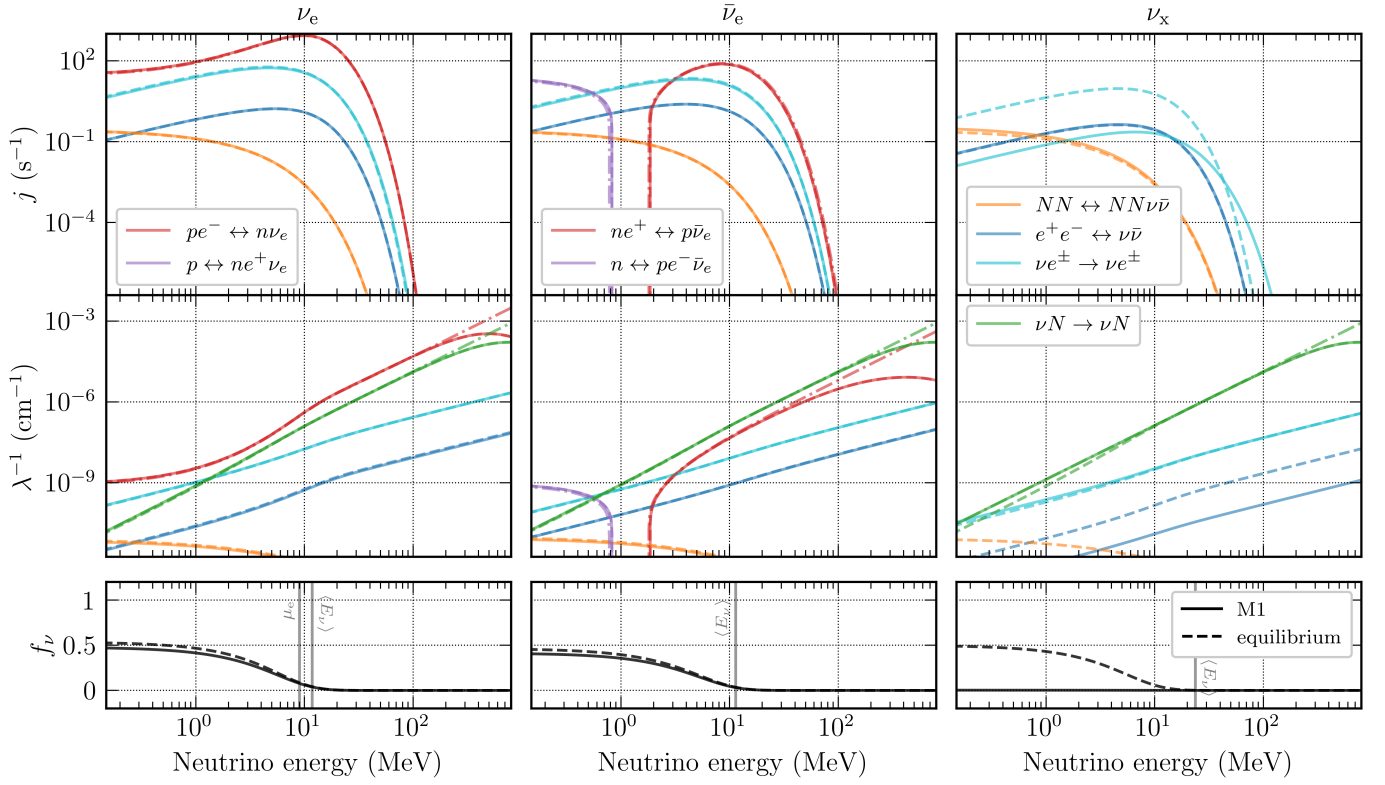


FIG. 15. Same as Fig. 3 but for thermodynamic point E in Table II.

- [23] O. Just, I. Kullmann, S. Goriely, A. Bauswein, H.-T. Janka, and C. E. Collins, *Mon. Not. Roy. Astron. Soc.* **510**, 2820 (2022), arXiv:2109.14617 [astro-ph.HE].
- [24] D. Radice and S. Bernuzzi, *Astrophys. J.* **959**, 46 (2023), arXiv:2306.13709 [astro-ph.HE].
- [25] F. Foucart, M. D. Duez, L. E. Kidder, R. Nguyen, H. P. Pfeiffer, and M. A. Scheel, *Phys. Rev.* **D98**, 063007 (2018), arXiv:1806.02349 [astro-ph.HE].
- [26] F. Foucart, P. C.-K. Cheong, M. D. Duez, L. E. Kidder, H. P. Pfeiffer, and M. A. Scheel, *Phys. Rev. D* **110**, 083028 (2024), arXiv:2407.15989 [astro-ph.HE].
- [27] P. L. Espino, D. Radice, F. Zappa, R. Gamba, and S. Bernuzzi, *Phys. Rev. D* **109**, 103027 (2024), arXiv:2311.12923 [astro-ph.HE].
- [28] P. C.-K. Cheong, F. Foucart, M. D. Duez, A. Offermans, N. Muhammed, and P. Chawhan, *Astrophys. J.* **975**, 116 (2024), arXiv:2407.16017 [astro-ph.HE].
- [29] A. Perego, D. Vescovi, A. Fiore, L. Chiesa, C. Vogl, S. Benetti, S. Bernuzzi, M. Branchesi, E. Cappellaro, S. Cristallo, A. Flörs, W. E. Kerzendorf, and D. Radice, *Astrophys. J.* **925**, 22 (2022), arXiv:2009.08988 [astro-ph.HE].
- [30] N. Domoto, M. Tanaka, S. Wanajo, and K. Kawaguchi, *Astrophys. J.* **913**, 26 (2021), arXiv:2103.15284 [astro-ph.HE].
- [31] L. Chiesa, A. Perego, and F. M. Guercilena, *Astrophys. J. Lett.* **962**, L24 (2024), arXiv:2311.17159 [astro-ph.HE].
- [32] S. Rosswog, E. Ramirez-Ruiz, and M. B. Davies, *Mon. Not. Roy. Astron. Soc.* **345**, 1077 (2003), arXiv:astro-ph/0306418 [astro-ph].
- [33] I. Zalamea and A. M. Beloborodov, *Mon. Not. Roy. Astron. Soc.* **410**, 2302 (2011), arXiv:1003.0710 [astro-ph.HE].
- [34] A. Perego, H. Yasin, and A. Arcones, *J. Phys.* **G44**, 084007 (2017), arXiv:1701.02017 [astro-ph.HE].
- [35] C. Musolino, L. Rezzolla, and E. R. Most, arXiv:2410.06253 [astro-ph.HE] (2024).
- [36] Y.-L. Zhu, A. Perego, and G. C. McLaughlin, *Phys. Rev. D* **94**, 105006 (2016), arXiv:1607.04671 [hep-ph].
- [37] M. Frensel, M.-R. Wu, C. Volpe, and A. Perego, *Phys. Rev. D* **95**, 023011 (2017), arXiv:1607.05938 [astro-ph.HE].
- [38] M.-R. Wu, I. Tamborra, O. Just, and H.-T. Janka, *Phys. Rev. D* **96**, 123015 (2017), arXiv:1711.00477 [astro-ph.HE].
- [39] M. George, M.-R. Wu, I. Tamborra, R. Ardevol-Pulpillo, and H.-T. Janka, *Phys. Rev. D* **102**, 103015 (2020), arXiv:2009.04046 [astro-ph.HE].
- [40] H. Nagakura, *Phys. Rev. D* **108**, 103014 (2023), arXiv:2306.10108 [astro-ph.HE].
- [41] E. Grohs, S. Richers, S. M. Couch, F. Foucart, J. Froustey, J. P. Kneller, and G. C. McLaughlin, *Astrophys. J.* **963**, 11 (2024), arXiv:2309.00972 [astro-ph.HE].
- [42] J. Froustey, S. Richers, E. Grohs, S. D. Flynn, F. Foucart, J. P. Kneller, and G. C. McLaughlin, *Phys. Rev. D* **109**, 043046 (2024), arXiv:2311.11968 [astro-ph.HE].
- [43] M. Cusinato, F. M. Guercilena, A. Perego, D. Logoteta, D. Radice, S. Bernuzzi, and S. Ansoldi, *European Physical Journal A* **58**, 99 (2022), arXiv:2111.13005 [astro-ph.HE].

- [44] Y. Sekiguchi, K. Kiuchi, K. Kyutoku, and M. Shibata, *Phys. Rev. D* **91**, 064059 (2015), arXiv:1502.06660 [astro-ph.HE].
- [45] R. Ardevol-Pulpillo, H. T. Janka, O. Just, and A. Bauswein, *Mon. Not. Roy. Astron. Soc.* **485**, 4754 (2019), arXiv:1808.00006 [astro-ph.HE].
- [46] F. Foucart, E. O'Connor, L. Roberts, M. D. Duez, R. Haas, L. E. Kidder, C. D. Ott, H. P. Pfeiffer, M. A. Scheel, and B. Szilagyi, *Phys. Rev. D* **91**, 124021 (2015), arXiv:1502.04146 [astro-ph.HE].
- [47] F. Foucart, E. O'Connor, L. Roberts, L. E. Kidder, H. P. Pfeiffer, and M. A. Scheel, *Phys. Rev. D* **94**, 123016 (2016), arXiv:1607.07450 [astro-ph.HE].
- [48] D. Radice, S. Bernuzzi, A. Perego, and R. Haas, *Mon. Not. Roy. Astron. Soc.* **512**, 1499 (2022), arXiv:2111.14858 [astro-ph.HE].
- [49] F. Schianchi, H. Gieg, V. Nedora, A. Neuweiler, M. Ujevic, M. Bulla, and T. Dietrich, *Phys. Rev. D* **109**, 044012 (2024), arXiv:2307.04572 [gr-qc].
- [50] C. Musolino and L. Rezzolla, *Mon. Not. Roy. Astron. Soc.* **528**, 5952 (2024), arXiv:2304.09168 [gr-qc].
- [51] P. C.-K. Cheong, H. H.-Y. Ng, A. T.-L. Lam, and T. G. F. Li, *Astrophys. J. Suppl.* **267**, 38 (2023), arXiv:2303.03261 [astro-ph.IM].
- [52] J. M. Miller, B. R. Ryan, J. C. Dolence, A. Burrows, C. J. Fontes, C. L. Fryer, O. Korobkin, J. Lippuner, M. R. Mumpower, and R. T. Wollaeger, *Phys. Rev. D* **100**, 023008 (2019), arXiv:1905.07477 [astro-ph.HE].
- [53] J. M. Miller, B. R. Ryan, and J. C. Dolence, *Astrophys. J. Suppl.* **241**, 30 (2019), arXiv:1903.09273 [astro-ph.IM].
- [54] F. Foucart, M. D. Duez, F. Hebert, L. E. Kidder, H. P. Pfeiffer, and M. A. Scheel, *Astrophys. J. Lett.* **902**, L27 (2020), arXiv:2008.08089 [astro-ph.HE].
- [55] F. Foucart, M. D. Duez, F. Hebert, L. E. Kidder, P. Kovarik, H. P. Pfeiffer, and M. A. Scheel, *Astrophys. J.* **920**, 82 (2021), arXiv:2103.16588 [astro-ph.HE].
- [56] F. Foucart, M. D. Duez, R. Haas, L. E. Kidder, H. P. Pfeiffer, M. A. Scheel, and E. Spira-Savett, *Phys. Rev. D* **107**, 103055 (2023), arXiv:2210.05670 [astro-ph.HE].
- [57] E. O'Connor, *Astrophys. J. Suppl.* **219**, 24 (2015), arXiv:1411.7058 [astro-ph.HE].
- [58] H. H.-Y. Ng, P. C.-K. Cheong, A. T.-L. Lam, and T. G. F. Li, *Astrophys. J. Suppl.* **272**, 9 (2024), arXiv:2309.03526 [astro-ph.HE].
- [59] S. Bacca, K. Hally, M. Liebendorfer, A. Perego, C. J. Pethick, and A. Schwenk, *Astrophys. J.* **758**, 34 (2012), arXiv:1112.5185 [astro-ph.HE].
- [60] L. F. Roberts, S. Reddy, and G. Shen, *Phys. Rev. C* **86**, 065803 (2012), arXiv:1205.4066 [astro-ph.HE].
- [61] G. Martínez-Pinedo, T. Fischer, A. Lohs, and L. Huther, *Phys. Rev. Lett.* **109**, 251104 (2012), arXiv:1205.2793 [astro-ph.HE].
- [62] L. F. Roberts and S. Reddy, *Phys. Rev. C* **95**, 045807 (2017), arXiv:1612.02764 [astro-ph.HE].
- [63] T. Fischer, G. Guo, A. A. Dzhiyev, G. Martínez-Pinedo, M.-R. Wu, A. Lohs, and Y.-Z. Qian, *Phys. Rev. C* **101**, 025804 (2020), arXiv:1804.10890 [astro-ph.HE].
- [64] G. Guo, G. Martínez-Pinedo, A. Lohs, and T. Fischer, *Phys. Rev. D* **102**, 023037 (2020), arXiv:2006.12051 [hep-ph].
- [65] M. Oertel, A. Pascal, M. Mancini, and J. Novak, *Phys. Rev. C* **102**, 035802 (2020), arXiv:2003.02152 [astro-ph.HE].
- [66] G. Guo, G. Martínez-Pinedo, and M.-R. Wu, *Phys. Rev. C* **110**, 015504 (2024), arXiv:2401.10737 [nucl-th].
- [67] H. H.-Y. Ng, C. Musolino, S. D. Tootle, and L. Rezzolla, arXiv:2411.19178 [astro-ph.HE] (2024).
- [68] P. C.-K. Cheong, F. Foucart, H. H.-Y. Ng, A. Offermans, M. D. Duez, N. Muhammed, and P. Chawhan, arXiv:2410.20681 [astro-ph.HE] (2024).
- [69] A. Perego, D. Radice, F. M. Guercilena, L. Chiesa, and M. Bhattacharyya, BNS\_NURATES (2025), [https://github.com/RelNucAs/bns\\_nurates](https://github.com/RelNucAs/bns_nurates).
- [70] S. W. Bruenn, *Astrophys. J. Suppl.* **58**, 771 (1985).
- [71] C. J. Horowitz, *Phys. Rev. D* **65**, 043001 (2002), arXiv:astro-ph/0109209.
- [72] M. Hempel, *Phys. Rev. C* **91**, 055807 (2015), arXiv:1410.6337 [nucl-th].
- [73] J. A. Pons, J. A. Miralles, and J. M. Ibanez, *Astron. Astrophys. Suppl. Ser.* **129**, 343 (1998), arXiv:astro-ph/9802333.
- [74] S. Hannestad and G. Raffelt, *Astrophys. J.* **507**, 339 (1998), arXiv:astro-ph/9711132.
- [75] T. Fischer, *Astron. Astrophys.* **593**, A103 (2016), arXiv:1608.05004 [astro-ph.HE].
- [76] A. Mezzacappa and S. W. Bruenn, *Astrophys. J.* **410**, 740 (1993).
- [77] A. Burrows, S. Reddy, and T. A. Thompson, *Nucl. Phys. A* **777**, 356 (2006), arXiv:astro-ph/0404432.
- [78] M. Shibata, K. Kiuchi, Y.-i. Sekiguchi, and Y. Suwa, *Prog. Theor. Phys.* **125**, 1255 (2011), arXiv:1104.3937 [astro-ph.HE].
- [79] H. Andresen, E. P. O'Connor, O. E. Andersen, and S. M. Couch, *Astron. Astrophys.* **687**, A55 (2024), arXiv:2402.18303 [astro-ph.HE].
- [80] I. Tamborra, B. Müller, L. Hudepohl, H.-T. Janka, and G. Raffelt, *Phys. Rev. D* **86**, 125031 (2012), arXiv:1211.3920 [astro-ph.SR].
- [81] G. N. Minerbo, *Journal of Quantitative Spectroscopy and Radiative Transfer* **20**, 541 (1978).
- [82] T. Fukushima, *Applied Mathematics and Computation* **259**, 708 (2015).
- [83] D. Radice and L. Rezzolla, *Astron. Astrophys.* **547**, A26 (2012), arXiv:1206.6502 [astro-ph.IM].
- [84] D. Radice, L. Rezzolla, and F. Galeazzi, *Class.Quant.Grav.* **31**, 075012 (2014), arXiv:1312.5004 [gr-qc].
- [85] D. Radice, L. Rezzolla, and F. Galeazzi, *Mon.Not.Roy.Astron.Soc.* **437**, L46 (2014), arXiv:1306.6052 [gr-qc].
- [86] F. Löffler, J. Faber, E. Bentivegna, T. Bode, P. Diener, R. Haas, I. Hinder, B. C. Mundim, C. D. Ott, E. Schnetter, G. Allen, M. Campanelli, and P. Laguna, *Class. Quantum Grav.* **29**, 115001 (2012), arXiv:1111.3344 [gr-qc].
- [87] Z. Etienne, S. R. Brandt, P. Diener, W. E. Gabella, M. Gracia-Linares, R. Haas, A. Kedia, M. Alcubierre, D. Alic, G. Allen, M. Ansorg, M. Babiuc-Hamilton, L. Baiotti, W. Benger, E. Bentivegna, S. Bernuzzi, T. Bode, G. Bozzola, B. Brendal, B. Bruegmann, M. Campanelli, F. Cipolletta, G. Corvino, S. Cupp, R. De Pietri, H. Dimmelmeier, R. Dooley, N. Dorband, M. Elley, Y. El Khamra, J. Faber, T. Font, J. Frieben, B. Giacomazzo, T. Goodale, C. Gundlach, I. Hawke, S. Hawley, I. Hinder, E. A. Huerta, S. Husa, S. Iyer, D. Johnson, T. Kellermann, A. Knapp, M. Kopitz, P. Laguna, G. Lanferman, F. Löffler, J. Masso,

- L. Menger, A. Merzky, J. Maxwell Miller, M. Miller, P. Moesta, P. Montero, B. Mundim, A. Nerozzi, S. C. Noble, C. Ott, R. Paruchuri, D. Pollney, D. Radice, T. Radke, C. Reisswig, L. Rezzolla, D. Rideout, M. Rippeanu, L. Sala, J. A. Schewtschenko, E. Schnetter, B. Schutz, E. Seidel, E. Seidel, J. Shalf, K. Sible, U. Sperhake, N. Stergioulas, W.-M. Suen, B. Szilagyi, R. Takahashi, M. Thomas, J. Thornburg, M. Tobias, A. Tonita, P. Walker, M.-B. Wan, B. Wardell, L. Werneck, H. Witek, M. Zilhão, B. Zink, and Y. Zlochower, *The Einstein Toolkit* (2021).
- [88] D. Pollney, C. Reisswig, E. Schnetter, N. Dorband, and P. Diener, *Phys. Rev.* **D83**, 044045 (2011), [arXiv:0910.3803 \[gr-qc\]](#).
- [89] C. Reisswig, C. D. Ott, E. Abdikamalov, R. Haas, P. Moesta, and E. Schnetter, *Phys. Rev. Lett.* **111**, 151101 (2013), [arXiv:1304.7787 \[astro-ph.CO\]](#).
- [90] S. Bernuzzi and D. Hilditch, *Phys. Rev.* **D81**, 084003 (2010), [arXiv:0912.2920 \[gr-qc\]](#).
- [91] D. Hilditch, S. Bernuzzi, M. Thierfelder, Z. Cao, W. Tichy, and B. Bruegmann, *Phys. Rev.* **D88**, 084057 (2013), [arXiv:1212.2901 \[gr-qc\]](#).
- [92] E. Schnetter, S. H. Hawley, and I. Hawke, *Class.Quant.Grav.* **21**, 1465 (2004), [arXiv:gr-qc/0310042 \[gr-qc\]](#).
- [93] C. Reisswig, R. Haas, C. D. Ott, E. Abdikamalov, P. Mösta, D. Pollney, and E. Schnetter, *Phys. Rev.* **D87**, 064023 (2013), [arXiv:1212.1191 \[astro-ph.HE\]](#).
- [94] M. J. Berger and J. Olinger, *J.Comput.Phys.* **53**, 484 (1984).
- [95] M. J. Berger and P. Colella, *Journal of Computational Physics* **82**, 64 (1989).
- [96] S. Typel, G. Ropke, T. Klahn, D. Blaschke, and H. H. Wolter, *Phys. Rev.* **C81**, 015803 (2010), [arXiv:0908.2344 \[nucl-th\]](#).
- [97] M. Hempel and J. Schaffner-Bielich, *Nucl. Phys.* **A837**, 210 (2010), [arXiv:0911.4073 \[nucl-th\]](#).
- [98] D. Radice, *Astrophys. J.* **838**, L2 (2017), [arXiv:1703.02046 \[astro-ph.HE\]](#).
- [99] D. Radice, *Symmetry* **12**, 1249 (2020), [arXiv:2005.09002 \[astro-ph.HE\]](#).
- [100] K. Kiuchi, K. Kyutoku, Y. Sekiguchi, and M. Shibata, *Phys. Rev.* **D97**, 124039 (2018), [arXiv:1710.01311 \[astro-ph.HE\]](#).
- [101] K. Kiuchi, S. Fujibayashi, K. Hayashi, K. Kyutoku, Y. Sekiguchi, and M. Shibata, *Phys. Rev. Lett.* **131**, 011401 (2023), [arXiv:2211.07637 \[astro-ph.HE\]](#).
- [102] E.ourgoulhon, P. Grandclement, K. Taniguchi, J.-A. Marck, and S. Bonazzola, *Phys.Rev.* **D63**, 064029 (2001), [arXiv:gr-qc/0007028 \[gr-qc\]](#).
- [103] T. A. Thompson, A. Burrows, and J. E. Horvath, *Phys. Rev. C* **62**, 035802 (2000), [arXiv:astro-ph/0003054](#).
- [104] C. R. Trott, D. Lebrun-Grandié, D. Arndt, J. Ciesko, V. Dang, N. Ellingwood, R. Gayatri, E. Harvey, D. S. Hollman, D. Ibanez, N. Liber, J. Madsen, J. Miles, D. Poliakoff, A. Powell, S. Rajamanickam, M. Simberg, D. Sunderland, B. Turcksin, and J. Wilke, *IEEE Transactions on Parallel and Distributed Systems* **33**, 805 (2022).
- [105] H. C. Edwards, C. R. Trott, and D. Sunderland, *Journal of Parallel and Distributed Computing* **74**, 3202 (2014), domain-Specific Languages and High-Level Frameworks for High-Performance Computing.
- [106] <https://www.nersc.gov/systems/perlmutter/>.
- [107] J. Fields, H. Zhu, D. Radice, J. M. Stone, W. Cook, S. Bernuzzi, and B. Daszuta, *Astrophys. J. Suppl.* **276**, 35 (2025), [arXiv:2409.10384 \[astro-ph.HE\]](#).
- [108] T. Fischer, S. Whitehouse, A. Mezzacappa, F.-K. Thielemann, and M. Liebendorfer, *Astron. Astrophys.* **517**, A80 (2010), [arXiv:0908.1871 \[astro-ph.HE\]](#).
- [109] L. Hudepohl, B. Muller, H. T. Janka, A. Marek, and G. G. Raffelt, *Phys. Rev. Lett.* **104**, 251101 (2010), [Erratum: *Phys.Rev.Lett.* **105**, 249901 (2010)], [arXiv:0912.0260 \[astro-ph.SR\]](#).
- [110] A. Betranhandy and E. O'Connor, *Phys. Rev. D* **102**, 123015 (2020), [arXiv:2010.02261 \[astro-ph.HE\]](#).
- [111] M. G. Alford and S. P. Harris, *Phys. Rev. C* **98**, 065806 (2018), [arXiv:1803.00662 \[nucl-th\]](#).
- [112] P. Hammond, I. Hawke, and N. Andersson, *Phys. Rev. D* **104**, 103006 (2021), [arXiv:2108.08649 \[astro-ph.HE\]](#).
- [113] E. R. Most and C. A. Raithel, *Phys. Rev. D* **104**, 124012 (2021), [arXiv:2107.06804 \[astro-ph.HE\]](#).
- [114] E. Dijkstra, *Numer. Math.* **1**, 269 (1959).